

Degradation models for hydrogen embrittlement

M. DADFARNIA and P. SOFRONIS,
University of Illinois at Urbana-Champaign, USA,
B. P. SOMERDAY and D. K. BALCH,
Sandia National Laboratories, USA and
P. SCHEMBRI, Los Alamos National Laboratory, USA

Abstract: In this chapter, we present a solid mechanics modeling and simulation effort to elucidate the linking of the macroscopic embrittlement phenomenology to the features of the microstructural degradation mechanisms ahead of a crack tip in the austenitic Fe–Ni–Co alloy IN903. In general, we find that the deformation and hydrogen fields in the fracture process depend strongly on the initial and boundary conditions, thus reflecting the variety of fracture modes. In particular, for intergranular crack growth in wedge opening load specimens in hydrogen gas we predict fracture process zones that are large in comparison to the typical characteristic diffusion distances. For ductile cracking in gaseous environments, we find that the process is controlled by the average spacing of the carbides.

Key words: hydrogen embrittlement, subcritical cracking, intergranular cracking, ductile fracture, grain boundary decohesion, void growth.

11.1 Introduction

Assessing the current status of understanding of hydrogen embrittlement of materials, we may state that research to date [1] has identified the nature of the hydrogen-induced degradation¹ mechanisms in almost all metals and alloys. By way of example, we mention that lately we began to understand even the very elusive concept of ‘quasi-cleavage’. Martin *et al.* [3] found that ‘quasi-cleavage’ in medium strength steels is a mechanism that is triggered and promoted exclusively by hydrogen-induced slip banding.

¹ We used in the chapter title the term degradation rather than the term damage because we believe that the latter misrepresents the nature of the hydrogen-induced failure. As Ahn *et al.* [2] report, hydrogen degradation is usually localized at a specific location where cracking initiates whereas the notion of damage points to distributed degradation, e.g., void formation in creeping materials at high temperatures in the neighborhood of a crack tip as dictated by local triaxiality.

However, we have not yet come up with fracture criteria that reflect a quantitative relationship between the degradation mechanisms and the macroscopic parameters that are used as indices of embrittlement [4]. Perhaps this is partly due to our lack of understanding of the specific relationship between the degradation mechanisms, the material microstructure, and the operating conditions. For instance, it is not known why and how the fracture mode depends on the hydrogen environment (gaseous vs. internal hydrogen), the magnitude of hydrogen pressure in the case of gaseous embrittlement, and the grain size. Summarizing the unresolved issues, Gangloff [5] states that several uncertainties still exist with regard to the hydrogen uptake and the interaction of the diffusible hydrogen with the stress and microstructural environment ahead of a crack tip.

An approach to elucidate the relationship between the materials science of the embrittlement phenomenon and the macroscopic indices of embrittlement is through modeling and simulation. We are in need of models which are predictive by relying on the specific hydrogen/microstructure interaction as observed through *in situ* microstructural analysis techniques. Further, we are in need of so-called ‘next generation’ models that (i) do not just assert the fact that embrittlement is a result of slip localization or decohesion and (ii) can be used to simulate material response at a level beyond the coupled interaction between material deformation and hydrogen diffusion. From a fracture performance prognosis standpoint, we are in need of models to (i) explain outstanding issues such as why the subcritical cracking thresholds at arrest and initiation differ in the case of mild strength steels; (ii) explore and establish criteria of environmental similitude between real-life components and laboratory specimens; and (iii) assess risk associated with potential variability of the microstructure (e.g. the formation or presence of additional hydrogen trapping microstructural features) or risk associated with third party damage (e.g. the significance of an external crack on the integrity of a hydrogen transportation pipeline).

Robust models of this nature can help elucidate hydrogen/material compatibility by providing information over a large number of issues:

- Important parameters influencing environmental similitude such as cyclic pressure profile and frequency for pipeline environments can be investigated perhaps in greater detail through simulation than through experiment.
- The timescales underscoring the kinetics issues in slow diffusivity systems such as the austenitic steels render the comprehensive experimental investigation of such parameters as subcritical cracking thresholds almost impractical to obtain. Modeling and simulation for such systems can be an invaluable tool toward predicting the material response over time periods that are decades long.

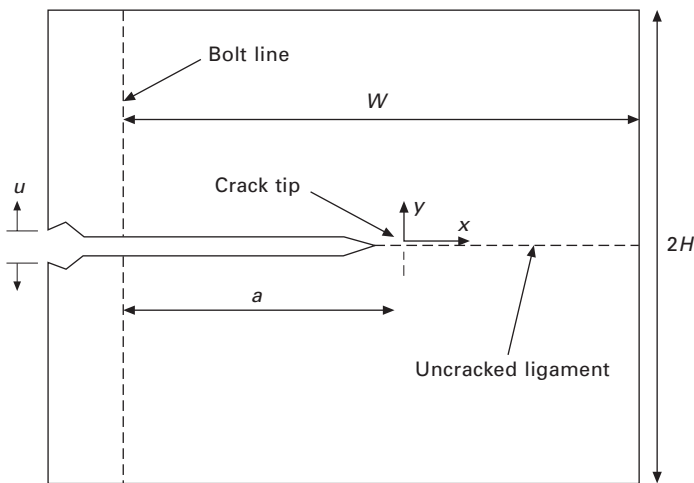
- Given the uncertainty surrounding the free surface conditions for hydrogen uptake, modeling can help elucidate the influence of the uptake kinetics on the operation of the degradation mechanism.

The present work aims to outline a modeling and simulation effort in the framework we discussed above. It addresses issues of coupling between hydrogen transport kinetics and the failure mechanisms as documented experimentally in the case of a Fe–Ni–Co superalloy IN903. For the quantitative description of the proposed models for the hydrogen-induced material degradation, we try to use parameters that were or can be determined by experiment or their magnitude can be assessed by atomistic simulation. For parameters that cannot be determined with certainty, we resort to parametric studies by judiciously bounding their magnitude. For instance, we deem that the magnitude of the grain boundary cohesive stress cannot exceed a large multiple of the macroscopic yield stress and that the hydrogen-induced degradation of grain boundary cohesion is not unlimited. In particular, simulating a crack tip environment, we link the mechanisms of hydrogen induced degradation at the microscale with the magnitude of the applied loads at the macroscale. We investigate issues related with the modeling of the hydrogen-induced failure when cracking proceeds either intergranularly or by a ductile mechanism. To quantify the failure load, we use in the case of intergranular cracking the cohesive element formalism to simulate grain boundary decohesion, whereas for cases in which failure is ductile, our approach relies on the hydrogen effect on void growth after nucleation. In the following, we discuss some of the results from the subcritical crack growth experiments of Moody *et al.* [6, 7] with the alloy IN903. The objective is to lay out the physics of our models and the embrittlement phenomenology they should simulate and predict.

To measure the resistance of high strength materials to hydrogen embrittlement [8], one can use either rising load testing or slow crack growth experiments under static loading [4, 9, 10]. The corresponding *initiation* and *arrest thresholds* which for high strength systems are usually similar [11] can be used for the safe and reliable design of structures and components operating in gaseous hydrogen environment. From a practical perspective, thresholds measured in the laboratory do not necessarily represent zero crack growth rate; rather, these thresholds may be associated with extremely low crack growth rates that are defined in part based on the resolution of the crack-detection instrumentation. In the present study, we explore how a solid mechanics approach can be used [12] to predict through modeling and simulation the threshold stress intensity factor for the case of subcritical cracking of IN903. For the validation of the predictions, we compare the simulation results against the experimental data of Moody *et al.* [6, 7] who investigated the response of the alloy IN903 under sustained-load cracking

with the use of the wedge opening load (WOL) specimen (see Fig. 11.1 for a schematic) that was either exposed to a high pressure hydrogen gaseous environment after it was bolt-loaded or hydrogen-precharged before loading. This Fe–base superalloy was solution treated at 940 °C, water quenched, and double-aged at 720 °C for 8 h and 620 °C also for 8 h. This treatment resulted in a microstructure [13] comprised equiaxed grains, $\sim 28\text{ }\mu\text{m}$ in diameter, strengthened by 20 nm γ' precipitates of nominal composition $\text{Ni}_3(\text{Ti}, \text{Al})$ at 10% by volume, and containing a significant number of annealing twins and matrix carbides at 0.3% by volume. The matrix carbides were predominantly $(\text{Nb}, \text{Ti})\text{C}$ with a few NbC and TiC . The average carbide size was $6.3\text{ }\mu\text{m}$ and their average spacing was $35\text{ }\mu\text{m}$. The grain boundaries were also decorated by MC or M_6C carbides.

Moody *et al.* [6, 7] associated near-threshold subcritical cracking of IN903 samples in hydrogen gas at pressures smaller than 45 MPa with ductile fracture mechanisms. For example, at 20.7 MPa hydrogen gas pressure, subcritical cracking took place by slip band fracture that originated at carbide particles while at 44.8 MPa, the fracture mode was mixed, consisting of slip band and intergranular failure. At higher hydrogen pressures, e.g. 100 MPa, subcritical cracking occurred entirely intergranularly. On the other hand, when precharged specimens were used, Moody *et al.* [6, 7] found that subcritical slip band cracking predominated in IN903 regardless of the hydrogen precharging pressure. These experimental results are indeed intriguing because they demonstrate the complexity of the hydrogen-induced failure mechanisms: the subcritical cracking mechanism depends not only on the hydrogen



11.1 Schematic of the wedge opening load (WOL) specimen. Bolt-loading induces a mouth opening displacement u . The crack size before hydrogen-induced propagation is a_0 .

boundary condition (external gaseous source vs. internal precharged source), but even for a given hydrogen source the mode of failure may depend on the particular magnitude of the parameters involved (e.g. hydrogen pressure in the case of gaseous embrittlement). Certainly we do not imply here that a parameter such as the hydrogen pressure is a critical parameter dictating directly the embrittlement mechanism. Rather, we understand this peculiar pressure effect as a phenomenological manifestation of the influence of the pressure on the attainment of potential criticality conditions for the onset of the embrittlement event.

11.2 Subcritical intergranular cracking under gaseous hydrogen uptake

11.2.1 On the use of the cohesive element formalism to simulate brittle fracture

Simulation of crack propagation using cohesive elements goes back to the work of Needleman [14]. Since then a great number of researchers used the cohesive element approach to study interfacial separation (e.g. Liang and Sofronis [15]; Serebrinsky *et al.* [16]) or ductile crack propagation (e.g. Tvergaard and Hutchinson [17]; Ruggieri *et al.* [18]). A thorough review of the numerical analysis of crack propagation methods and their relevance to hydrogen-induced crack growth is presented by Ahn *et al.* [2]. Liang and Sofronis [15, 19, 20] used cohesive elements to study the effect of hydrogen on void nucleation and grain boundary decohesion in the nickel–base alloy 690. They simulated hydrogen-induced interfacial separation on the basis of the thermodynamic theory of decohesion put forward by Hirth and Rice [21]. Based on the structure of the traction separation law as derived from the deformation of a unit cell that involved a decohering particle, Liang and Sofronis [15] proposed a means of estimating the hydrogen-induced reduction in the energy spent on fracture initiation for alloy 690 in a way that correlates with the reduction in the fracture toughness of the material as measured by macroscopic experiments. The interaction of hydrogen transport with material atomic cohesion and brittle failure ahead of a crack tip in bcc iron was investigated by Serebrinsky *et al.* [16]. Scheider *et al.* [22] studied crack growth of a high strength low alloy steel in ASTM substitute ocean water environment. They determined the magnitude of the parameters describing the cohesive element properties by fitting the simulated crack propagation behavior to experimental results.

In the present work, we model and simulate hydrogen-induced intergranular crack propagation in the alloy IN903 along the lines set by Dadfarnia *et al.* [12]. In that work, Dadfarnia *et al.* aimed at predicting the threshold stress intensity factor by modeling the debonding of the grain boundaries through

cohesive finite elements. The relevant traction-separation law was determined on the basis of the thermodynamic theory of decohesion by Mishin *et al.* [23] and its parameters were calibrated through *ab initio* calculations. In the present work, we try to come up with an assessment of the use of the cohesive element methodology in predicting threshold stress intensity factors in the high strength alloy IN903.

11.2.2 Thermodynamics of intergranular decohesion

Following Mishin *et al.* [23], we consider a planar grain boundary experiencing a uniform separation δ under a normal tensile stress σ_{int} while hydrogen atoms diffuse in the created open space (Fig. 11.2). In this model, the grain boundary is treated as a thermodynamic system described by a given set of parameters denoting certain phenomenological characteristics such as energy and critical separation. The state of the grain boundary can be characterized by the hydrogen coverage (H atoms per metal atom) $c_{\text{int}} = \theta_{\text{int}}\beta_{\text{int}} = C_{\text{int}}/N_{\text{int}}$, where N_{int} denotes the number of metal atoms per unit area, β_{int} the available interstitial sites per host grain boundary atom, θ_{int} the occupancy of the interstitial sites, and C_{int} is hydrogen coverage of the boundaries measured in H atoms per unit grain boundary area. We write the Helmholtz free energy f of the grain boundary (energy per metal atom) as

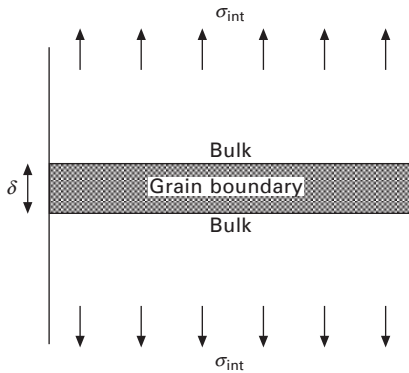
$$df = \sigma_{\text{int}}/N_{\text{int}} d\delta + \mu_{\text{int}} dc_{\text{int}} \quad [11.1]$$

where the chemical potential of a hydrogen atom μ_{int} on the grain boundary is given by

$$\mu_{\text{int}} = (\partial f / \partial c_{\text{int}})_{\delta} \quad [11.2]$$

and the opening stress by

$$\sigma_{\text{int}} = N_{\text{int}} (\partial f / \partial \delta)_{c_{\text{int}}} \quad [11.3]$$



11.2 Grain boundary separation distance δ under applied stress σ_{int} .

A convenient form for the free energy is

$$f(c_{\text{int}}, \delta) = \varepsilon(c_{\text{int}}) + \varphi(c_{\text{int}}, \delta) + \beta_{\text{int}} k \Theta [\theta_{\text{int}} \ln \theta_{\text{int}} + (1 - \theta_{\text{int}}) \ln(1 - \theta_{\text{int}})] \quad [11.4]$$

where $\varepsilon(c_{\text{int}})$ denotes the surface energy (completely separated grain boundary), $\varphi(c_{\text{int}}, \delta)$ represents the cohesive energy of the boundary, $k = R/N_A$ is Boltzmann's constant with $R = 8.314 \text{ J/mol K}$ being the universal gas constant and $N_A = 6.0232 \times 10^{23}$ atoms/mol Avogadro's number, and Θ is the absolute temperature. The last term in Eq. (11.4) is the free energy density due to the configurational entropy of the hydrogen atoms on the grain boundary in the ideal solution approximation. As a first approximation, we assume linear interpolations for the forms $\varepsilon(c_{\text{int}})$ and $\varphi(c_{\text{int}}, \delta)$, that is,

$$\varepsilon(c_{\text{int}}) = (1 - c_{\text{int}}/c_c) \varepsilon_A + (c_{\text{int}}/c_c) \varepsilon_B \quad [11.5]$$

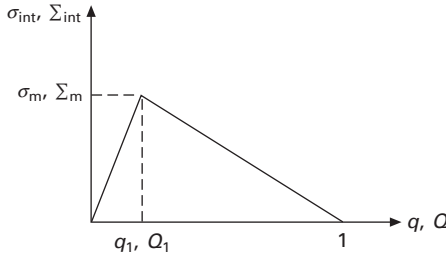
$$\varphi(c_{\text{int}}, \delta) = (1 - c_{\text{int}}/c_c) \varphi_A(\delta) + (c_{\text{int}}/c_c) \varphi_B(\delta) \quad [11.6]$$

where $\varphi_A(\delta)$ and ε_A are respectively the cohesive energy and twice the surface energy of the pure grain boundary in the absence of hydrogen, and $\varphi_B(\delta)$ and ε_B are corresponding parameters when the grain boundary is fully saturated with hydrogen ($\theta_{\text{int}} = 1$) at concentration $c_c = \beta_{\text{int}}$. We further assume that $\varphi_A(\delta) = \varphi_A^0 g(q)$ and $\varphi_B(\delta) = \varphi_B^0 g(q)$, where φ_A^0 and φ_B^0 are respectively the zero-stress cohesive energies of the hydrogen-free and fully H-saturated grain boundary. For the dimensionless function,² we consider the form

$$g(q) = \begin{cases} 1 - \frac{q^2}{q_1} & 0 \leq q \leq q_1 \\ \frac{(1-q)^2}{(1-q_1)} & q_1 \leq q \leq 1 \\ 0 & 1 \leq q \end{cases} \quad [11.7]$$

in which $q = \delta/\delta_c$ is the normalized separation of the grain boundary under stress and δ_c is the critical separation upon failure. We assume zero equilibrium separation in the absence of stress. We chose the form of the function $g(q)$ in Eq. (11.7) such that at constant grain boundary hydrogen concentration c_{int} , Eq. (11.3) yields a grain boundary stress, σ_{int} , that increases with separation linearly up to separation q_1 and then decreases linearly to zero at separation $q = 1$ (Fig. 11.3). Using the form of Eq. (11.6), one finds from Eqs. (11.2)

² In an earlier version of this thermodynamic theory, Dadfarnia *et al.* [12] used a polynomial form for $g(q)$ for which the cohesive stress was always attained at normalized separation $q_1 = 1/3$. In the present work, we opted for a more versatile model for $g(q)$ in which q_1 is treated as a separate parameter input in order to explore the interaction of the compliance of the grain boundary with the bulk material deformation.



11.3 Traction-separation law at fixed grain boundary hydrogen concentration c_{int} . Parameters indicated by lower and upper case symbols are respectively for reversible and irreversible grain boundary separation. The critical separations δ_c and Δ_c correspondingly for reversible and irreversible separations are used to nondimensionalize the corresponding separations δ and Δ such that $q = \delta/\delta_c$ and $Q = \Delta/\Delta_c$.

through (11.4) the chemical potential of hydrogen on the grain boundary measured in J/mol

$$\mu_{int} = \frac{N_A(\varepsilon_B - \varepsilon_A)}{c_c} + \frac{N_A\varphi_A^0(\kappa - 1)}{c_c} g(q) + R\Theta \ln \frac{c_{int}}{\beta_{int} - c_{int}} \quad [11.8]$$

and the grain boundary stress

$$\sigma_{int}(c_{int}, q) = \frac{N_{int}\varphi_A^0}{\delta_c} [1 + (\kappa - 1)c_{int}/c_c] \frac{\partial g(q)}{\partial q} \quad [11.9]$$

where $\kappa = \varphi_B^0/\varphi_A^0$ denotes the ratio of the cohesive energy of the stress-free grain boundary at full hydrogen coverage ($\theta_{int} = 1$) to that in the absence of hydrogen ($\theta_{int} = 0$). Dadfarnia *et al.* [12, 24] report a value for $\kappa = \varphi_B^0/\varphi_A^0$ equal to 0.85 on the basis of *ab initio* calculations with $\Sigma 3$ grain boundary interfaces (i.e., a grain boundary with high atomic registry). Such a value indicates that hydrogen can reduce the cohesive energy of grain boundaries at saturation by as much as 15%. This reduction is certainly dependent on the grain boundary structure we considered and its ability to accommodate hydrogen. One may conjecture that a grain boundary with less atomic registry could yield a larger reduction of the cohesive energy by hydrogen. However, direct experimental evidence for marked reductions is still lacking, and as we show in this work, hydrogen can drive intergranular fracture even in the absence of large reductions of cohesion.

The reversible work of separation of the grain boundary, γ_{int} , is calculated through

$$2\gamma_{int} = \delta_c \int_{(c_0, q=0)}^{(c_d, q=1)} \sigma_{int}(c_{int}, q) dq \quad [11.10]$$

where c_d is the hydrogen concentration at complete decohesion ($q = 1$) and c_0 is the zero-stress grain boundary hydrogen concentration. When separation is fast and takes place at constant hydrogen concentration c_{int} , Eqs. (11.7), (11.9), and (11.10) yield for the reversible work of separation

$$(2\gamma_{\text{int}})_{c_{\text{int}}} = -N_{\text{int}}\phi_A^0 \left[1 + (\kappa - 1) \frac{c_{\text{int}}}{c_c} \right] \quad [11.11]$$

In the absence of hydrogen ($c_{\text{int}} = 0$), Eqs. (11.9) and (11.11) yield

$$\sigma_{\text{int}}(c_{\text{int}} = 0, q) = \frac{N_{\text{int}}\phi_A^0}{\delta_c} \frac{\partial g(q)}{\partial q} \quad [11.12]$$

for the grain boundary stress and

$$(2\gamma_{\text{int}})_0 = \int_0^{\delta_c} \sigma_{\text{int}}(0, \delta) d\delta = \delta_c \int_0^1 \sigma_{\text{int}}(0, q) dq = -N_{\text{int}}\phi_A^0 \quad [11.13]$$

for the reversible work of separation. Lastly, from Eqs. (11.11) and (11.13), we find

$$\kappa = \frac{(2\gamma_{\text{int}})_{c_c}}{(2\gamma_{\text{int}})_0} = \frac{\text{reversible work of separation}|_{\theta_{\text{int}}=1}}{\text{reversible work of separation}|_{\theta_{\text{int}}=0}} \quad [11.14]$$

The grain boundary stress σ_{int} attains its maximum σ_m at $q = q_1$, which we term grain boundary cohesive stress

$$\sigma_m(c_{\text{int}}) = -2 \frac{N_{\text{int}}\phi_A^0}{\delta_c} \left[1 + (\kappa - 1) \frac{c_{\text{int}}}{c_c} \right] \quad [11.15]$$

Using Eqs. (11.11) and (11.12), one can readily show

$$(2\gamma_{\text{int}})_{c_{\text{int}}} = \frac{1}{2} \sigma_m(c_{\text{int}}) \delta_c, \quad (2\gamma_{\text{int}})_0 = \frac{1}{2} (\sigma_m)_0 \delta_c \quad [11.16]$$

where $(\sigma_m)_0 = \sigma_m(c_{\text{int}} = 0)$ is the cohesive stress in the absence of hydrogen.

11.2.3 Hydrogen transport

Bulk material (grain interior)

We assume that hydrogen diffusion in the bulk material takes place through normal interstitial lattice sites (NILS). We also allow in our model for the possibility that diffusible hydrogen is trapped at microstructural defects [25]. We assume that the populations of the hydrogen solute atoms residing at NILS and reversible trapping sites are always in equilibrium. According to Oriani's equilibrium theory [26], one can relate the occupancy θ_T of the trapping sites to the occupancy θ_L of the NILS through $\theta_T/(1 - \theta_T) = \theta_L/$

$(1 - \theta_L)K_T$, where $K_T = \exp(W_B/R\Theta)$ denotes the equilibrium constant and W_B is the trap binding energy. The hydrogen concentration C_L in NILS, measured in hydrogen atoms per unit volume, can be expressed as $C_L = \theta_L \beta N_L$, where β denotes the number of NILS per solvent atom, and N_L denotes the number of solvent atoms per unit volume given by $N_L = N_A/V_M$ with V_M being the molar volume of the host lattice measured in units of volume per mole. Similarly, the concentration of hydrogen in trapping sites, C_T , measured in hydrogen atoms per unit volume, can be phrased as $C_T = \theta_T \alpha N_T$, where α denotes the number of sites per trap and N_T denotes the trap density in number of traps per unit volume. We assume that trapping takes place at the interface between the matrix and the γ' precipitates. These precipitates, whose presence is characterized by an extremely large density, would dominate the trapped hydrogen population development even in the presence of other trap states such as dislocations [13]. Certainly the present model of trapping can be modified to account for other trap states such as grain boundaries or dislocations [27]; for the case of trapping at dislocations the trap density $N_T = N_T(\epsilon^p)$ is a function of the amount of the local plastic strain ϵ^p . Lastly, although the trap populations are calculated to be comparable to those in NILS, trapping in the bulk of the grain may not affect the kinetics of the embrittlement through a reduced effective diffusivity because in this face centered cubic (fcc) nickel structure the lattice diffusion by itself is very slow compared with that in body centered cubic (bcc) structures.

Conservation of diffusible and trapped hydrogen requires

$$\frac{D}{D_{\text{eff}}} \frac{\partial C_L}{\partial t} + J_{i,i} = 0 \quad [11.17]$$

where $()_{,i} = \partial()/\partial x_i$, $\partial/\partial t$ denotes partial differentiation with respect to time, D is the hydrogen diffusion coefficient through NILS, $D_{\text{eff}} = D/(1 + \partial C_T/\partial C_L)$ is an effective diffusion coefficient, J_i is the i th component of the hydrogen flux vector

$$J_i = -\frac{DC_L}{R\Theta} \mu_{,i} \quad [11.18]$$

in which

$$\mu = \mu^0 + R\Theta \ln \theta_L - \frac{\sigma_{kk} V_H}{3} \quad [11.19]$$

is the chemical potential of hydrogen in NILS, μ^0 is the chemical potential in the standard state, σ_{ij} is the Cauchy stress, V_H is the partial molar volume of hydrogen in solid solution, and the standard summation convention over the range is implied for a repeated index.

Grain boundary diffusion

Hydrogen diffusion along grain boundaries which undergo decohesion is governed by

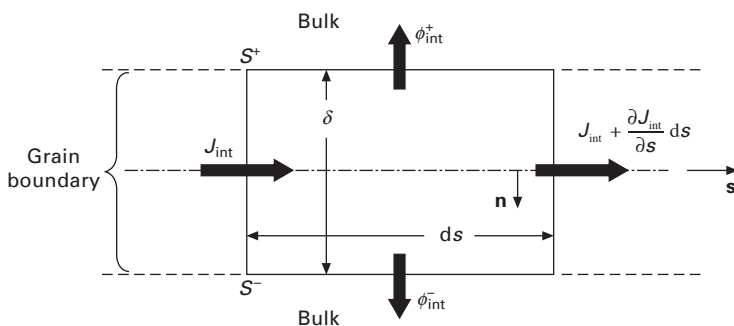
$$J_{\text{int}} = - \frac{D_{\text{int}} C_{\text{int}}}{R\Theta} \frac{\partial \mu_{\text{int}}}{\partial s} \quad [11.20]$$

where J_{int} is the flux measured in number of hydrogen atoms per unit width of the grain boundary per unit time (see Fig. 11.4), D_{int} is the grain boundary diffusion coefficient of hydrogen, and s is distance along the grain boundary. With reference to Fig. 11.4, conservation of diffusible hydrogen along the grain boundary dictates

$$\frac{dC_{\text{int}}}{dt} + \frac{dJ_{\text{int}}}{ds} + \phi_{\text{int}}^+ + \phi_{\text{int}}^- = 0 \quad [11.21]$$

where ϕ_{int}^+ and ϕ_{int}^- are the hydrogen fluxes away from the grain boundary through the upper side S^+ and lower side S^- , respectively. As hydrogen diffuses along the grain boundary and through the NILS sites in the bulk, there is a continuous exchange of hydrogen atoms between the grain boundary and the adjacent bulk NILS such that continuity of the chemical potential of hydrogen across the boundary is maintained. From the expressions for the chemical potential of hydrogen given by Eqs. (11.8) and (11.19), we find

$$\frac{\theta_{\text{int}}}{1 - \theta_{\text{int}}} = \theta_L S_m S_q \quad [11.22]$$



11.4 Schematic of an infinitesimal element of a separating grain boundary. Hydrogen flux J_{int} is measured in hydrogen atoms diffusing in the direction \mathbf{s} along the grain boundary per unit time per unit grain boundary width in direction $\mathbf{s} \times \mathbf{n}$. Fluxes ϕ_{int}^+ and ϕ_{int}^- denotes hydrogen atoms per unit area per unit time away from the grain boundary.

where

$$S_q = \exp \left\{ \left[-\frac{N_A \phi_A^0 (\kappa - 1)}{c_c} [g(q) - 1] - \sigma_{kk} V_H / 3 \right] / R\Theta \right\} \quad [11.23]$$

and

$$S_m = \exp \left\{ \left[\mu^0 - \frac{N_A (\varepsilon_B - \varepsilon_A)}{c_c} - \frac{N_A \phi_A^0 (\kappa - 1)}{c_c} \right] / R\Theta \right\} \quad [11.24]$$

Eq. (11.22) for the relationship between occupancies θ_{int} and θ_L is a side constraint that we enforce in the simulation of concurrent hydrogen diffusion along the grain boundaries and through the bulk material (grain interior) as dictated by the corresponding chemical potential gradients given by Eqs. (11.8) and (11.19).

The parameter S_q is a function of the grain boundary opening and hydrostatic stress in the bulk. In the absence of stress ($\sigma_{kk} = 0$ and $q = 0$), $S_q = 1$ and hence Eq. (11.22) reduces to $\theta_{\text{int}} / (1 - \theta_{\text{int}}) = S_m \theta_L$. One easily observes that the parameter S_m is the equilibrium constant relating the occupancy of the interstitial lattice sites in the bulk to the occupancy of the sites in the grain boundary. As such, it can be re-phrased as

$$S_m = \exp(W_{\text{int}}/R\Theta) \quad [11.25]$$

where W_{int} is the binding energy of hydrogen to the grain boundary. Specifically for the alloy IN903, the dependence of θ_{int} on θ_L through S_m and S_q is further discussed on pages 345–6.

Using Eq. (11.22), we find that the chemical potential continuity across the grain boundary requires that the hydrogen concentration on the grain boundary C_{int} and the hydrogen concentration C_L in the adjacent bulk NILS are related through

$$C_{\text{int}} = \frac{\beta_{\text{int}} N_{\text{int}} S_m S_q C_L}{\beta N_L + S_m S_q C_L}$$

11.2.4 Constitutive model

Bulk material (grain interior)

We assume that the bulk material surrounding the grain boundary crack deforms elastically and for the sake of simplicity in the finite element calculations linearly and isotropically. In other words, we are modeling intergranular failure of the alloy IN903 as taking place in the absence of any substantive plastic deformation in the bulk. This assumption is based on a calculation of the plastic zone as the crack propagates which shows that the plasticity

is confined in a zone 14-grain wide and containing the crack face. In fact, as we explain in the next subsection, we model and account for any plastic dissipation in the narrow zone around the grain boundary that is attendant to the grain boundary failure through the traction-separation law we adopt to characterize the mechanical response of the grain boundary. Since IN903 is a high solubility system, we account for the hydrogen induced dilatation [28] by considering a contribution D_{ij}^h

$$D_{ij}^h = \frac{d}{dt} \left\{ \ln \left[1 + \frac{(c - c_0)\Delta v}{3\Omega} \right] \right\} \delta_{ij} \quad [11.26]$$

to the total deformation rate (symmetric part of the velocity gradient), where c is the total hydrogen concentration in both lattice and trapping sites, c_0 is the initial hydrogen concentration in the stress-free material, $\Delta v = V_H/N_A$ is the volume increase per hydrogen atom introduced into solution, $\Omega = 1/N_L$ is the mean atomic volume of the host metal atom, and δ_{ij} is the Kronecker delta.

Grain boundary

In subsection 11.2.3, we presented a thermodynamic theory to describe the cohesive properties of the grain boundaries. The theory provides formulae for the description of the reversible work of separation, e.g., Eq. (11.10), and the related stress, Eq. (11.9), as functions of separation and hydrogen coverage during the decohesion process. This form of traction-separation law could be used to describe the cohesive properties of the grain boundary only if the fracture was ideally brittle. In the case of IN903, the subcritical cracking we are modeling involves substantial plastic dissipation despite the fact that fracture progresses intergranularly. For instance, Moody *et al.* [6, 7] measured an arrest threshold $K_{th} = 33 \text{ MPa} \sqrt{\text{m}}$ in 207 MPa gaseous hydrogen with a specimen loaded before the onset of crack propagation at $K_I^0 = 57.8 \text{ MPa} \sqrt{\text{m}}$. These stress intensity factors are associated with plastic dissipation exceeding the grain boundary cohesive energy by at least three orders of magnitude, although cracking proceeded intergranularly. More generally, addressing the nature of brittle fracture, Jokl *et al.* [29] demonstrated convincingly that plastic shearing almost invariably accompanies brittle decohesion. Moreover, Jokl *et al.* came up with a quantitative description of the plastic work expended upon decohesion as a function of the reversible work of fracture.

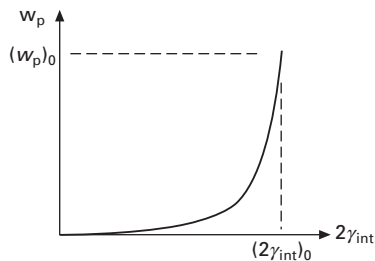
In this work, we account for the plastic dissipation expended upon intergranular fracture by following the approach of Jokl *et al.* [29]. We stipulate that plastic work w_p is expended upon grain boundary separation through local shearing processes taking place in a very narrow zone around the

grain boundaries. Supporting evidence for such a grain boundary separation scenario may be found in the work of Lillig [30] in the case of Ni_3Al and the work of Lee *et al.* [31] in the case of a Ni–S alloy. Reviewing the subject, Robertson *et al.* [1] maintains that hydrogen-driven intergranular fracture was observed in their transmission electron microscopy (TEM) studies to occur ‘with significant dislocation activity at and in advance of the propagating crack.’ We are assuming that this work expenditure is localized to the grain boundaries, or else fracture (taking place with widely spread plasticity) would not be macroscopically brittle, that is, of low energy. Hence, we do not identify this localized plastic work with the work expended in forming the standard macroscopic plastic zone that develops ahead of a crack tip in the case of ductile fractures. We view plastic work w_p as work attendant to the intergranular separation event. As such, we account for it in the description of the traction-separation law we are devising for the simulation of the grain boundary decohesion.

Following Jokl *et al.* [29], Lin *et al.* [32], and Novak *et al.* [27], we consider that the total work expended upon intergranular separation is the sum of the reversible work of fracture and the attendant plastic dissipation

$$w = w_p + 2\gamma_{\text{int}} \quad [11.27]$$

in which w_p is a function of $2\gamma_{\text{int}}$. We are assuming a dependence of w_p on $2\gamma_{\text{int}}$ characterized by a very steep slope as shown schematically in Fig. 11.5 in accordance with the calculations of Jokl *et al.* [29]. Jokl *et al.* concluded that such a steep-slope feature can be used to explain the abrupt change in the macroscopic mode of failure, often observed in the case of environmental fractures, from ductile to brittle. Teter *et al.* [33] and Novak *et al.* [27] relied precisely on this steep-slope feature to rationalize hydrogen-induced decohesion. Of course, there may be other approaches that can lead to the same rationalization such as large hydrogen accumulations at a fracture initiation site. The interesting feature of our present approach is that it does



11.5 The irreversible (plastic) work of fracture as a function of the reversible work. The subscript ‘0’ denotes quantity in the absence of hydrogen.

not require large hydrogen accumulations; instead, it is based on the nature of the functional relationship between plastic dissipation and reversible work for failure. Given the lack of experimental or computational data, we propose the following form for the plastic dissipation upon fast separation

$$(w_p)_{c_{\text{int}}} = (w_p)_0 \left[\frac{(2\gamma_{\text{int}})_{c_{\text{int}}}}{(2\gamma_{\text{int}})_0} \right]^m \quad [11.28]$$

where m is an integer exponent. The parameter $(w_p)_0$ denotes attendant plastic work in the absence of hydrogen if fracture were intergranular. However, we note that intergranular cracking in the absence of hydrogen is an inaccessible fracture mode for alloy IN903 since it fails by ductile processes that involve void nucleation at carbides followed by growth and coalescence [6, 7]. In our simulation approach, the parameter $(w_p)_0$ represents the limit case of no hydrogen for which all plastic dissipation ahead of the crack tip is lumped onto $(w_p)_0$ with the total work of fracture being $(w)_0 = (w_p)_0 + (2\gamma_{\text{int}})_0 = J_{\text{IC}}$. The parameter J_{IC} is the fracture toughness of the material in the absence of hydrogen expressed in terms of the J -integral. Certainly the magnitude of $(w_p)_0$ as calibrated in terms of $(2\gamma_{\text{int}})_0$ and J_{IC} is in accord with the standard cohesive zone formalism for ductile fracture whereby J_{IC} is the magnitude of work expended along the entire cohesive zone upon *crack initiation* [34]. In this context,

$$(w)_0 = \Delta_c \int_0^1 \Sigma_{\text{int}} dQ \quad [11.29]$$

where Σ_{int} is the grain boundary traction for intergranular separation in the presence of attendant plastic dissipation, $Q = \Delta/\Delta_c$ is normalized grain boundary separation, and Δ_c is the critical separation upon decohesion. Thus $(w)_0$ denotes the area underneath the traction separation law $\Sigma_{\text{int}} - \Delta$ in the absence of hydrogen as shown in Fig. 11.3 in terms of the normalized separation.

Once the crack begins to advance intergranularly in the presence of hydrogen, the grain boundary cohesive properties change continuously depending on the hydrogen coverage of the grain boundaries. In order to quantitatively describe the effect of hydrogen on the traction separation law, we follow Liang and Sofronis [20] and assume that at any instant of time during decohesion the process is very fast whereby one can assume that instantaneously $c = c_{\text{int}}$. Thus, we suggest that at any location ahead of the propagating crack

$$(w)_{c_{\text{int}}} = \Delta_c \int_0^1 \Sigma_{\text{int}}(c_{\text{int}}, Q) dQ \quad [11.30]$$

where the total work of fracture $(w)_{c_{\text{int}}}$ also satisfies Eq. (11.27) with $2\gamma_{\text{int}}$

and w_p replaced with $(2\gamma_{\text{int}})_{c_{\text{int}}}$ and $(w_p)_{c_{\text{int}}}$, respectively. Of course, as time evolves and the hydrogen coverage of the decohering interface at any location along the grain boundary changes, so does $(w)_{c_{\text{int}}}$ and in turn the traction-separation law.

Similar to the case of reversible decohesion (see Fig. 11.3), we propose to describe the traction separation law at constant hydrogen grain boundary coverage c_{int} through a triangular form

$$\Sigma_{\text{int}}(c_{\text{int}}, Q) = \begin{cases} \Sigma_m(c_{\text{int}})(Q/Q_1) & Q < Q_1 \\ \Sigma_m(c_{\text{int}})(1 - Q)/(1 - Q_1) & Q_1 < Q < 1 \\ 0 & Q > 1 \end{cases} \quad [11.31]$$

where $\Sigma_m(c_{\text{int}})$ is the cohesive stress (see Fig. 11.3). As with the parameter $(w_p)_0$ which characterizes an inaccessible intergranular fracture mode in the absence of hydrogen, the cohesive stress $(\Sigma_m)_0 = \Sigma_m(c_{\text{int}} = 0)$ characterizes the strength of the grain boundary if fracture were to occur intergranularly in the absence of hydrogen. Thus, when $c_{\text{int}} = 0$, we continue to use in the simulations the traction separation law (11.31) as a limit case which though, as we discussed, is compatible with the cohesive zone approach to modeling ductile crack initiation. From Eqs. (11.29), (11.30) and (11.31), we find

$$(w)_{c_{\text{int}}} = \frac{1}{2} \Sigma_m(c_{\text{int}}) \Delta_c, \quad (w)_0 = \frac{1}{2} (\Sigma_m)_0 \Delta_c \quad [11.32]$$

In the numerical simulations for the grain boundary decohesion, we explore the effect of the traction separation law by setting the cohesive stress in the absence of hydrogen equal to a multiple of the yield stress of the material, $(\Sigma_m)_0 = \lambda \sigma_0$. Then from $(w)_0 = J_{\text{IC}}$ and the second of Eqs. (11.32), we calculate in the absence of hydrogen the critical separation distance Δ_c for decohesion. Then for any hydrogen coverage of the grain boundaries c_{int} , we determine the traction separation law as follows:

- Eq. (11.11) provides the reversible work of separation $(2\gamma_{\text{int}})_{c_{\text{int}}}$.
- Eq. (11.28) provides the associated plastic dissipation $(w_p)_{c_{\text{int}}}$ which is then used to calculate the total work for decohesion of the grain boundaries through $(w)_{c_{\text{int}}} = (w_p)_{c_{\text{int}}} + (2\gamma_{\text{int}})_{c_{\text{int}}}$.
- Given the magnitude of $(w)_{c_{\text{int}}}$, the first of Eqs. (11.32) furnishes the cohesive stress $\Sigma_m(c_{\text{int}})$ for given c_{int} .

Thus at any location along the grain boundary with H coverage, c_{int} , the traction separation law is defined as in Fig. 11.3 through $\Sigma_m(c_{\text{int}})$ and Δ_c .

11.2.5 Simulation of intergranular cracking under constant macroscopic displacement

Model parameters

We simulate intergranular cracking of the alloy IN903 which Moody *et al.* [6, 7] investigated with WOL specimens at hydrogen gas pressure 207 MPa and room temperature (295 K). Under these conditions the equilibrium concentration of hydrogen in both NILS and trapping sites on the crack flanks was 6135 appm. This concentration was calculated by Moody *et al.* [7] through the use of the Sievert's law for the concentration of hydrogen in NILS and the equilibrium relationship between hydrogen concentration in the γ' precipitates and NILS. In the experiments, the hydrogen-free specimen was first bolt-loaded to a given front-face crack opening displacement u (see Fig. 11.1) with an associated stress intensity factor K_I^0 [10] and the subsequent crack propagation in hydrogen gas was then monitored in time to identify the arrest threshold. In one case, the mouth opening was $u = 0.5588$ mm with an associated stress intensity factor $K_I^0 = 57.8$ MPa $\sqrt{\text{m}}$. Crack arrest took place after the crack propagated for about 19.17 mm over 20 days. In another case with $u = 0.8686$ mm and $K_I^0 = 81.0$ MPa $\sqrt{\text{m}}$, crack arrest took place after the crack propagated for about 20.52 mm over 60 h. In both experiments, the threshold stress intensity factor was calculated to be about $K_{\text{th}} = 33$ MPa $\sqrt{\text{m}}$.

We use a simulation domain that models the actual specimen used in the experiments: a 22.2 mm thick WOL specimen with height $2H = 55.4$ mm, width $W = 56.9$ mm (Fig. 11.1) and initial crack size to width ratio $a_0/W = 0.471$. Owing to symmetry, we model only the upper half of the specimen. To model the dominance of the hydrogen uptake through the crack faces and the crack tip, we assume that the specimen is hydrogen-free at time zero. On the crack flanks, we prescribe an NILS hydrogen concentration that is in equilibrium with the hydrogen gas pressure according to Sievert's law modified to account for fugacity [35]. Hence, we enforce $C_L = C_0 = 1.68 \times 10^{26}$ H atoms/m³ (=1953 appm) at all times. It should be noted that this equilibrium lattice concentration yields a total (NILS and trapping site) hydrogen concentration of 6135 appm, as reported by Moody *et al.* [7]. As the crack propagates and fresh surface is exposed to hydrogen gas, we assume that hydrogen equilibrium is rapidly established on the created surface. In other words, we ignore any surface reaction control [36] on crack propagation. On the outer boundary of the specimen, we prescribe a zero hydrogen concentration instead of C_0 given that the nature (concentration or flux) or the magnitude of the boundary condition at the remote boundary of the specimen has no effect on the solution close to the crack tip. The diffusivity of hydrogen in IN903 is so small that the crack tip hydrogen population development is affected only by the crack tip boundary

condition. We assume the grain boundaries to be located along the uncracked ligament (Fig. 11.1) with cohesive finite elements arrayed over the entire ligament.

At any given location ahead of the propagating crack tip and any instant of time at which the hydrogen coverage is c_{int} , we determine the traction separation law, $\Sigma_{\text{int}} - Q$, for the corresponding cohesive element as we outline in subsection 11.2.4 by accounting for the plastic dissipation. Since we solve the hydrogen transport equations incrementally in time, we update the traction-separation law following the update of c_{int} after each incremental step. For the simulation of the hydrogen transport along the grain boundary we assumed $q = Q$. In other words, we assumed that the normalized opening of the grain boundary is the same regardless of whether separation takes place under reversible conditions (subsection 11.2.2 on the description of deformation-driven hydrogen transport along the grain boundary) or under irreversible conditions (subsection 11.2.4 for the derivation of the traction-separation law in the presence of plastic dissipation). This allows the use of Q , as calculated in the presence of plastic dissipation, in the place of q in Eq. (11.8) for the chemical potential of the hydrogen atoms on the grain boundaries and in turn in Eqs. (11.20) and (11.21), respectively for the hydrogen flux and hydrogen conservation along the grain boundaries. We consider the cohesive stress $\sigma_m(c_{\text{int}})$ under reversible separation equal to the calculated $\Sigma_m(c_{\text{int}})$ under irreversible separation. On the other hand the critical separation distance Δ_c , under the irreversible conditions at which the crack propagation simulation is carried out, is not equal to the corresponding critical distance δ_c if decohesion was reversible, as can be surmised from Eqs. (11.16) and (11.32).

The magnitudes of the parameters we used in the simulation are listed in Table 11.1. We assumed a value 0.8 for the parameter κ that represents the ratio of the reversible work of separation for a hydrogen-saturated grain boundary to a hydrogen-free grain boundary. This assumption implies that the cohesive energy under reversible separation is reduced by hydrogen by as much as 20%. Certainly such a reduction of the cohesive stress, while it is not excessively large, is in accord with recent *ab initio* calculations of the order of magnitude of the hydrogen-induced cohesive energy reduction of a $\Sigma 3[1\bar{1}0](111)$ grain boundary in bcc iron [24]. In fact the *ab initio* calculations furnished a 15% maximum reduction at saturation. For the ideal cohesive energy of the grain boundary in the absence of hydrogen we assumed $\varphi_A^0 = -1.016 \times 10^{-18}$ J/atom, in line with the *ab initio* calculations with the model $\Sigma 3[1\bar{1}0](111)$ grain boundary, namely $\varphi_A^0 = -(\gamma_{\text{int}})_{c_{\text{int}}=0}/N_{\text{int}}$ in which $N_{\text{int}} = 2.56 \times 10^{18}$ atoms/m² [12]. Thus, the reversible work of decohesion in the absence of hydrogen is $(\gamma_{\text{int}})_{c_{\text{int}}=0} = 2.598$ J/m².

The diffusion coefficient of hydrogen through the NILS of the bulk material surrounding the propagating crack is $D = 1.66 \times 10^{-15}$ m²/s at 295 K [37]. With

Table 11.1 Material properties of IN903

Properties	Symbol	Value
Young's modulus	E	147.5 GPa
Poisson's ratio	ν	0.234
Yield stress	σ_0	1081 MPa
Work hardening exponent	n	0.047
Number of sites per trap	α	1
Number of NILS per host atom	β	1
Density of solvent atoms	N_L	8.603×10^{28} atoms/m ³
Trap density of γ' precipitates	N_T	$0.005 \times N_L$
Trap binding energy at γ' precipitates	W_B	19.3 kJ/mol (= 0.2 eV)
Molar volume of host metal	V_M	7.0 cm ³ /mol
Partial molar volume of H	V_H	1.73 cm ³ /mol
Diffusion coefficient	D	1.66×10^{-15} m ² /s
Lattice parameter	a	0.358 nm
Host metal atoms per unit grain boundary area	N_{int}	2.56×10^{18} atoms/m ²
Available grain boundary sites for hydrogen occupancy per metal atom	β_{int}	1
Ratio of cohesive grain boundary energies: hydrogen-saturated to hydrogen-free	κ	0.8
Exponent relating the plastic work for fracture to the reversible work of decohesion	m	10
Reversible work for grain boundary separation in the absence of hydrogen	$(2\gamma_{\text{int}})_0$	2.5978 J/m ²
Grain boundary binding energy	W_{int}	20.5 kJ/mol

regard to the grain boundary diffusion, D_{int} , we emphasize that our model predictions depend strongly on its magnitude. Assessing the literature, one notices that there is a debate about its magnitude for nickel and nickel–base alloys [38, 39]. Tsuru and Latanision [40] used secondary ion mass spectrometry (SIMS) analysis to interpret H permeation and concluded that grain boundaries enhance the diffusion of hydrogen. Kimura and Birnbaum [39], analyzing the experimental data of the kinetics of intergranular fracture of nickel, found that the magnitude of the grain boundary diffusion coefficient in nickel is less than 10 times the NILS diffusion coefficient. On the other hand, Yao and Cahoon [38] discuss conditions – e.g., grain boundary thickness – under which D_{int} can be orders of magnitude greater than D . However, later work by Cahoon and coworkers [41–43] suggests that there is no substantive difference between the grain boundary and the bulk diffusion coefficients in nickel.

Latanision *et al.* [44] reported that fast grain boundary diffusion of hydrogen in nickel–base alloys is unlikely. Permeation experiments by Robertson [45] in nickel and Latanision and Kurkela [46] in nickel and nickel–base alloys indicate that there is no measurable effect of grain size on hydrogen diffusivity. Ladna and Birnbaum [47] using SIMS studied the distribution of hydrogen

at grain boundaries of nickel bicrystals. They observed enhanced hydrogen diffusion along high energy 39° $\langle 110 \rangle$ symmetrical tilt boundaries ($\Sigma = 9$) but not along low energy 129° $\langle 110 \rangle$ symmetric tilt boundaries ($\Sigma = 11$). Mutschele and Kirchheim [48] and Kirchheim *et al.* [49], studying hydrogen segregation at grain boundaries and interfaces in palladium, concluded that the grain boundary diffusion coefficient is concentration dependent: smaller than the value for the single crystal at low hydrogen concentration, and larger at higher concentrations. A concentration dependence of the grain boundary coefficient in nickel has also been reported by Yao and Cahoon [41]. Looking at the assessment of the literature sources on the grain boundary diffusion of hydrogen in nickel by Sutton and Balluffi [50], one may conclude that the grain boundary diffusion coefficient is not larger by more than one order of magnitude than the lattice diffusion coefficient. Our assessment is that the discussion at this stage is not quantitatively conclusive [51] and the grain boundary diffusion coefficient is probably larger than D but not by a factor greater than 10. Thus, we opted to explore the effect of the relative magnitude between the two diffusion coefficients through parametric studies for the ratio D_{int}/D .

Before proceeding with the presentation of the finite element simulation results, we present an assessment of the relationship (11.22) that we use to enforce continuity of the chemical potential across the grain boundary. Also, this equation dictates the relationship between the hydrogen coverage of the grain boundary and the adjacent bulk material (cf. Eq. 11.26). With $W_{\text{int}} = 20.5 \text{ kJ/mol}$ being the binding energy of hydrogen to the grain boundary in the absence of straining, Eq. (11.25) yields $S_m = \exp(W_{\text{int}}/R\Theta) = 4264$ for the stress-free and perfectly bonded grain boundary. For a stress-free and completely decohered grain boundary ($q = 1$), we find through Eq. (11.23) that $S_m S_q = 1.96 \times 10^{25} = \exp(142.844 \text{ (kJ/mol)}/R\Theta)$ at room temperature. Comparing this result with Eq. (11.22), we deduce that the effective binding energy of hydrogen to the grain boundary upon decohesion can become as large as $W_{\text{int}} = 143 \text{ kJ/mol}$. This is a direct consequence of the thermodynamic model for the chemical potential of the grain boundary (Eq. 11.8) whereby the grain boundary's potential for attracting hydrogen atoms increases with increasing separation. Next we assess the magnitude of the product $S_m S_q$ in Eq. (11.22) for various values of the grain boundary separation q and normalized hydrostatic stress $\sigma_{kk}/3\sigma_0$ representative of the straining and stress environment which the separating grain boundary experiences. Given that $S_m = 4264$, we focus on S_q as defined by Eq. (11.23). Tables 11.2 and 11.3 show such values of S_q respectively for q_1 equal to 0.025 and 0.5 – for the calculations we assumed that the traction separation law attains its maximum value (see Fig. 11.3) at normalized separation q_1 .

Tables 11.2 and 11.3 show that for the dependence of S_q on the magnitudes of the grain boundary separation and the hydrostatic stress ahead of the

Table 11.2 Magnitude of the parameter S_q evaluated through Eq. (11.23) for various values of normalized grain boundary separation q and normalized hydrostatic stress $\sigma_{kk}/3\sigma_0$ in the grain. The maximum grain boundary stress (cohesive stress) is attained at $q_1 = 0.025$ (see Fig. 11.3)

q	$\sigma_{kk}/3\sigma_0$	S_q
0.01	0.0	1.22
0.01	0.75	0.69
0.01	1.5	0.39
0.025	3.0	0.35
0.025	10.0	0.0017
0.05	3.0	4.14
0.05	10.0	0.020
0.1	3.0	470.53
0.1	10.0	2.26
0.2	3.0	2.81×10^6
0.2	10.0	1.35×10^5

Table 11.3 Magnitude of the parameter S_q evaluated through Eq. (11.23) for various values of normalized grain boundary separation q and normalized hydrostatic stress $\sigma_{kk}/3\sigma_0$ in the grain. The maximum grain boundary stress (cohesive stress) is attained at $q_1 = 0.5$ (see Fig. 11.3)

q	$\sigma_{kk}/3\sigma_0$	S_q
0.05	0.3	1.02
0.05	0.6	0.81
0.2	1.5	17.12
0.5	3.0	6.80×10^9
0.5	10.0	3.31×10^7
0.75	0.3	4.20×10^{18}

crack tip, it is the grain boundary separation that has the strongest effect on S_q . This is particularly demonstrated by the bottom two rows of Tables 11.2 and 11.3. Thus away from the crack tip, where the separation q is small, we expect S_q to be small. Given the slow lattice diffusion of hydrogen in IN903 and hence the resulting small hydrogen amounts, as indicated through θ_L , traveling parallel to the grain boundary through the grain, continuity of the chemical potential dictates that the grain boundary concentrations at locations far away from the crack tip are markedly small. At the crack tip where the NILS occupancy is large, $\theta_L^0 = 0.00195$ at an external hydrogen pressure 207 MPa; then, $\theta_{\text{int}}^0 = 0.893$ in the absence of stress. Far from the crack tip, coverage θ_{int} reduces to zero. This will have significant consequences on the rate of crack propagation as we discuss next.

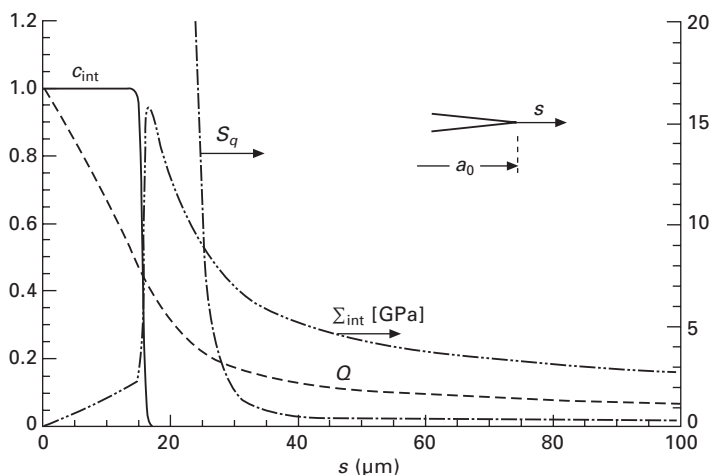
Numerical results

As hydrogen diffuses along the separating grain boundary and through the NILS sites in the bulk material surrounding the propagating crack, there is a continuous exchange of hydrogen atoms between the grain boundary and the adjacent bulk NILS such that continuity of the chemical potential of hydrogen across the interface is maintained. This provides the coupling between concurrent hydrogen transport through the bulk and along the grain boundaries. The coupled bulk-diffusion and grain-boundary diffusion problems are solved under the side constraint of chemical potential continuity across the grain boundary as in the work of Liang and Sofronis [19]. In addition, the solution to the hydrogen transport is coupled to the material deformation both in the bulk and in the form of hydrogen-induced crack propagation. The details of the finite element implementation can be found in the work of Dadfarnia [52]. For the calculations, we used a total of 26430 four-noded isoparametric elements to discretize the entire WOL specimen with a fine mesh around the propagating crack tip. The size of the crack tip bulk element bordering the corresponding cohesive element was $40\text{ }\mu\text{m}$. The crack propagated along the line designated as uncracked ligament in Fig. 11.1. The line was discretized with 1540 cohesive elements with sizes ranging from $5\text{ }\mu\text{m}$ at the crack tip before crack propagation to $40\text{ }\mu\text{m}$ at crack arrest.

We explored hydrogen-induced crack propagation by assuming that the cohesive stress of the grain boundaries is $(\Sigma_m)_0 = 18.5\text{ }\sigma_0 = 20.0\text{ GPa}$ in the absence of hydrogen, where σ_0 is the yield stress. This is indeed a substantially large cohesive stress when compared with the value of $\sim 3.5\text{ }\sigma_0$ that is typically used in the simulations of *R*-curve response [2]. We chose such a large cohesive stress in order to investigate the stress effect on driving intergranular failure. We note that although we assumed that the bulk material behaves elastically, utilizing cohesive elements ahead of the crack tip removes the crack tip singularity as the stresses cannot exceed the cohesive stress Σ_m (see Fig. 11.3). Also such a large cohesive stress magnitude is justified on the grounds that the bulk of the grain remains elastic and as such it can sustain stresses that can be excessively larger than those predicted by classical continuum plasticity theory. Large stresses in the nanometer region surrounding the crack tip have been sought by Gangloff [5] to explain hydrogen-induced decohesion in IN903 and a number of other high strength alloys. In fact, Gangloff [5] considered that strain gradient theories of plasticity may be used to justify the fracture requirement for normal stress elevations at the crack tip in excess of those predicted by classic theory. Later, for comparison purposes, we also report simulations with a cohesive stress $4\sigma_0$. For $(\Sigma_m)_0 = 20\text{ GPa}$, the second of Eqs. (11.32), yields $\Delta_c = 5.19\text{ }\mu\text{m}$. Also, we assumed $Q_1 = q_1 = 0.5$ (Fig. 11.3). In the simulations, the time is

measured from the time the macroscopic displacement is applied, that is, the applied stress intensity factor is K_I^0 .

Figure 11.6 shows the profiles of the hydrogen concentration c_{int} in H atoms per metal atom, grain boundary stress Σ_{int} , normalized grain boundary separation Q , and parameter S_q ahead of the crack tip upon the onset of crack propagation plotted against distance s from the crack tip along the axis of symmetry of the specimen after about 27 mins from the application of the macroscopic displacement associated with $K_I^0 = 57.8 \text{ MPa } \sqrt{\text{m}}$. Recall that S_q represents the adjacent hydrostatic stress and interface separation dependencies of H coverage of grain boundary sites, with a value of 1.0 denoting the stress free case. Upon the onset of crack propagation, we observe the formation of a hydrogen saturated ($c_{\text{int}} = 1.0$) plateau ahead of the crack tip of size $14 \mu\text{m}$. We also observe a rapid decrease of the magnitude of S_q with distance from the crack because S_q is a strong function of the grain boundary separation Q (see Table 11.3 or Eq. (11.23) with Q taken equal to the reversible q). The presence of these large concentrations ahead of the crack tip degrades the grain boundary cohesion, thus causing the crack to propagate. After the onset of crack propagation, the stress intensity the crack tip experiences reduces, and the crack advances in a crack tip environment associated with lesser applied stress and local-boundary stress. Hence, for



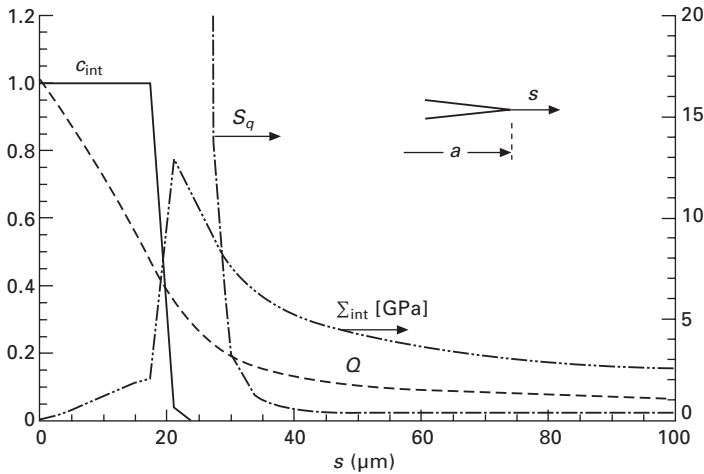
11.6 Profiles ahead of the crack tip upon onset of crack propagation after 27 min from bolt-loading the WOL specimen at $K_I^0 = 57.8 \text{ MPa } \sqrt{\text{m}}$ in a hydrogen gas environment (external embrittlement). The grain boundary cohesive stress is $(\Sigma_m)_0 = 20 \text{ GPa}$, the grain boundary diffusion coefficient is equal to the diffusion coefficient through NILS, $D_{\text{int}} = D$, the exponent in the relation between the plastic work of fracture and the reversible work is $m = 10$, and a_0 is the crack size prior to propagation.

continued crack growth in the simulations under decreasing applied stress intensity, a larger segment of the grain boundary needs to be degraded by hydrogen, that is, the resistance of the grain boundaries needs to be reduced over a longer distance from the crack tip than was the case at the onset. This necessitates a longer plateau saturated with hydrogen for continued crack propagation.

The physical picture of fracture implied from these results is that a larger fracture process zone is required for continued crack propagation, which is somewhat counterintuitive. One may reason out such a fracture scenario as follows. Continued crack growth under decreasing applied stress intensity factor can take place: (i) either through hydrogen degrading a larger volume of material (larger fracture process zone) under the given degradation intensity described by the proposed thermodynamic model of decohesion upon grain boundary saturation or (ii) by an increasing hydrogen-induced degradation of the cohesive stress if the size of the fracture process zone remains the same. The latter case would require grain boundaries that do not saturate with hydrogen; instead they continue to attract hydrogen beyond what is allowed by the physical space available. Given the fact that our material model is based on saturable grain boundaries and finite hydrogen-induced degradation upon grain boundary saturation (e.g. hydrogen at saturation reduces the reversible work of separation only by as much as 20%), the fracture scenario that can provide continued crack propagation in the simulations is that of a continuously increasing fracture process zone. We are inclined to accept this fracture scenario of an increasing fracture process zone given the fact that there is no direct experimental evidence of diminishing grain boundary cohesion upon hydrogen saturation.

Figure 11.7 shows the same profiles as Fig. 11.6 at time $t = 14$ h after the crack propagated by 2 mm and the applied stress intensity factor dropped to $K_I = 54.4 \text{ MPa} \sqrt{\text{m}}$. The hydrogen saturated plateau is now $17 \mu\text{m}$. The fact that the size of the plateau is required to increase as the crack advances implies that hydrogen has to diffuse longer distances as the crack propagates. This slows down the crack propagation rate. The crack which advances at ever decreasing velocities gets arrested when the grain boundary stress ahead of the crack tip is lower than the grain boundary resistance $\Sigma(c_{\text{int}})$. Figure 11.8 shows the profiles of hydrogen concentration c_{int} , grain boundary stress Σ_{int} , normalized grain boundary separation Q , and parameter S_q after the crack propagated 17 mm to arrest, and after 55 years elapsed from time zero. Looking at Figs 11.6 through 11.8, we state that the parameter S_q being small away from the crack tip³ is not the reason why crack propagation takes

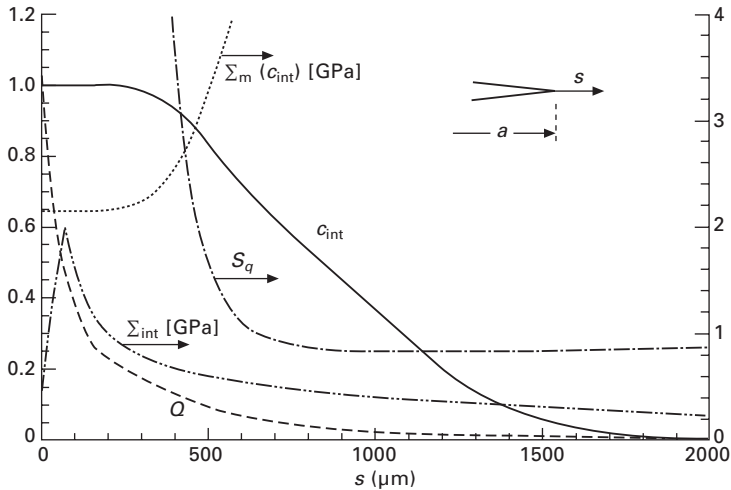
³ As we discussed on pages 345–6, a small value of S_q is associated with low hydrogen occupancies and hence low hydrogen coverage.



11.7 Profiles ahead of the crack tip after the crack propagated distance $a - a_0 = 2.0\text{ mm}$ over 14 h from loading the specimen at $K_I^0 = 57.8\text{ MPa}\sqrt{\text{m}}$ in hydrogen gas at pressure 207 MPa (external embrittlement). The grain boundary cohesive stress is $(\Sigma_m)_0 = 20\text{ GPa}$, $D_{\text{int}} = D$ and $m = 10$. The parameters a and a_0 denote current and prior to propagation crack sizes, respectively.

place at ever-decreasing rates. Certainly the profile of S_q ahead of the crack tip when the crack arrested is not qualitatively different from those at the early stages. Rather, we attribute the crack arrest to the requirement for an ever-increasing size of the saturation plateau for continued crack growth. Thus, as the applied stress intensity decreases by crack propagation, the associated normal tensile stress Σ_{int} (see Fig. 11.8) is not large enough to induce the crack to propagate along the grain boundaries and this is despite the fact that the cohesive stress Σ_m (see Fig. 11.8) has been reduced by the hydrogen effect in accordance with the thermodynamic model of grain boundary decohesion we proposed. As a result, the crack arrests and the corresponding stress intensity factor is designated as the arrest threshold. We note here that the plotted magnitudes of Σ_{int} and Σ_m as functions of distance from the crack tip are results of the simulations and reflect the complex interaction between straining, applied load, hydrogen transport, and the hydrogen effect as described by the present thermodynamic model.

Figure 11.9(a) shows the experimental results of Moody *et al.* [6, 7] for crack propagation as a function of time when the WOL specimen was loaded at fixed displacement to achieve $K_I^0 = 57.8\text{ MPa}\sqrt{\text{m}}$. Superposed on the figure are the numerical results for cohesive stress $(\Sigma_m)_0 = 18.5\sigma_0$ and also for $(\Sigma_m)_0 = 4\sigma_0$ ($\Delta_c = 24.0\mu\text{m}$, $Q_1 = 0.5$). Figure 11.9(b) shows the crack growth rate as a function of the applied stress intensity factor. Clearly, the

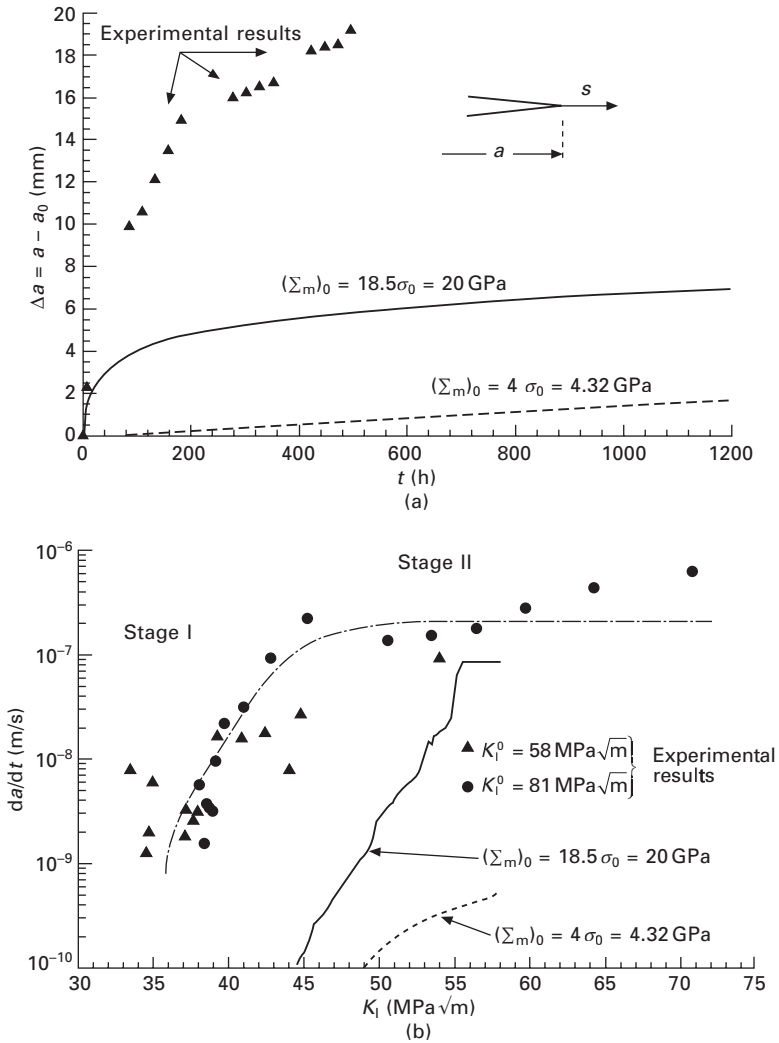


11.8 Profiles ahead of the crack tip long (55 years) after the crack propagated distance $a - a_0 = 17.0$ mm and arrested ($K_{th} = 36.6 \text{ MPa} \sqrt{\text{m}}$). The specimen was initially loaded to $K_I^0 = 57.8 \text{ MPa} \sqrt{\text{m}}$ in hydrogen gas at pressure 207 MPa (external embrittlement). The grain boundary cohesive stress is $(\Sigma_m)_0 = 20 \text{ GPa}$, $D_{int} = D$, and $m = 10$.

simulation results are markedly apart from the experimental results. Despite this difference, the calculated threshold stress intensity factor $K_{th} = 36.6 \text{ MPa} \sqrt{\text{m}}$ is close to the experimentally measured value of $33.5 \text{ MPa} \sqrt{\text{m}}$. The magnitude of the cohesive stress has a dramatic effect on the rate of crack propagation as shown in Fig. 11.9(b)⁴. With a larger cohesive stress, a smaller hydrogen-saturated plateau size is required for the necessary degradation of material resistance in order for the crack to advance. A smaller size plateau needs less time to be built and hence larger crack propagation velocities are the case. Looking at Fig. 11.9(b), one sees that the present model simulations do not provide a crack growth rate picture that exhibits the stage I and stage II regimes characterizing the experimental data. Rather the model provides a stage I type of response through a combination of applied stress intensity factor and hydrogen diffusion; the model does not display the diffusion-controlled, K -independent stage II regime. The reason is the requirement for an increased saturation plateau size as the crack advances.

Additional numerical simulations show that the calculated threshold stress intensity factor does not depend on the initial bolt loading (mouth opening displacement of the WOL specimen). For instance, calculations with initial

⁴ The experimental data show stage II crack growth rates of about $2 \times 10^{-7} \text{ m/s}$ as reported by Somerday and Moody [53] and Gangloff [5].



11.9 (a) Crack advance vs time as a function of cohesive stress $(\Sigma_m)_0$ in the absence of hydrogen. The parameter a_0 is the initial crack size prior to propagation. In both experiments and simulations, the specimen was bolt-loaded at $K_I^0 = 57.8$ MPa \sqrt{m} in hydrogen gas at pressure 207 MPa (external embrittlement). In the simulations, $D_{int} = D$ and $m = 10$. (b) Crack growth rate vs. applied stress intensity based on the experimental data (data points) and numerical simulations for grain boundary cohesive stresses of 20 and 4.32 GPa. The simulation data were obtained with $K_I^0 = 57.8$ MPa \sqrt{m} .

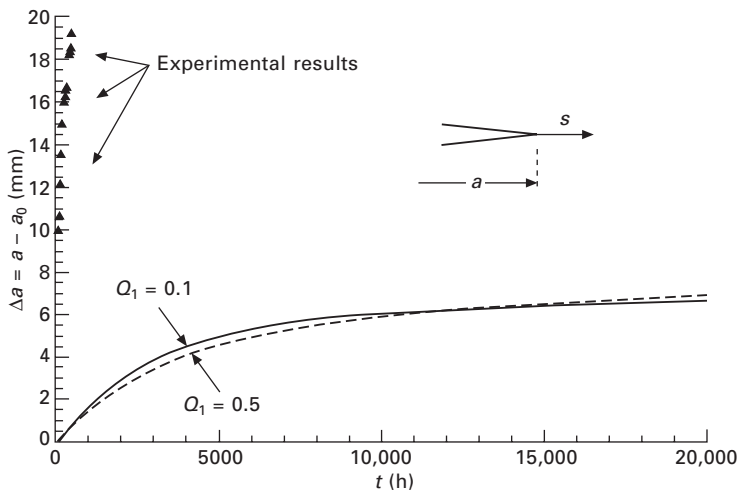
stress intensity factor $K_I^0 = 50 \text{ MPa}\sqrt{\text{m}}$ yield a similar threshold value of $40 \text{ MPa}\sqrt{\text{m}}$.

To investigate the dependence of the numerical results on the finite element size and the marching time step for hydrogen transport, we used finer mesh lay-outs and smaller time increments. The results we reported so far, although quantitatively slightly sensitive to the mesh size, are qualitatively independent of the finite element size and the marching time step.

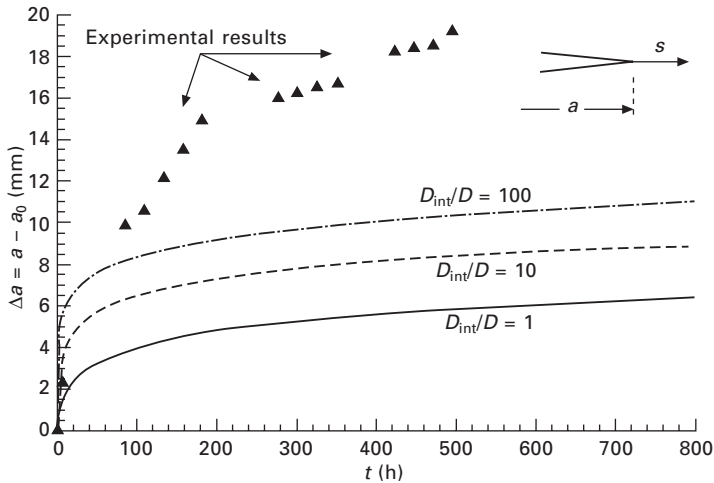
Parameter sensitivity of simulation results

To investigate the effect of the stiffness of the traction-separation law upon grain boundary opening on crack propagation, we carried out simulations by varying the parameter Q_1 when the cohesive stress is $(\Sigma_m)_0 = 4\sigma_0$. Figure 11.10 shows that the magnitude of Q_1 has a minimal effect on crack propagation velocity. This is in agreement with the work of Tvergaard and Hutchinson [17] in which they found that the shape of the traction separation law, as long as the maximum stress and the work of separation remain the same, has a relatively weak effect on the crack propagation velocity.

Figure 11.11 shows the effect of the grain boundary diffusion coefficient D_{int} on crack propagation while the bulk hydrogen diffusion coefficient D is kept constant as reported in Table 11.1. Clearly, faster diffusion along the grain boundaries accelerates crack growth at the early stages and improves agreement with the experimental velocities. In addition, we find in the



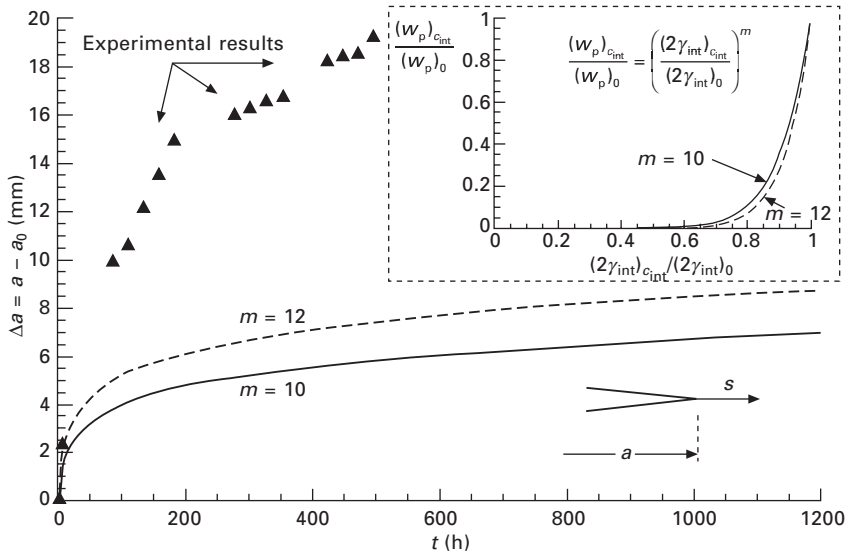
11.10 Effect of the parameter Q_1 (see Fig. 11.3) on crack propagation when the cohesive stress is $(\Sigma_m)_0 = 4\sigma_0$. In both experiments and simulations, the specimen was bolt-loaded at $K_I^0 = 57.8 \text{ MPa}\sqrt{\text{m}}$ in hydrogen gas at pressure 207 MPa (external embrittlement). In the simulations, $D_{\text{int}} = D$ and $m = 10$.



11.11 Sensitivity of crack growth to the grain boundary diffusion coefficient D_{int} when the cohesive stress is $(\Sigma_m)_0 = 20$ GPa. In both experiments and simulations, the specimen was bolt-loaded at $K_I^0 = 57.8 \text{ MPa}\sqrt{\text{m}}$ in hydrogen gas at pressure 207 MPa (external embrittlement). In the simulations, $m = 10$. The bulk hydrogen diffusion coefficient is $D = 1.66 \times 10^{-15} \text{ m}^2/\text{s}$.

simulations that crack is always arrested after 17 mm of growth regardless of the magnitude of the grain boundary diffusion coefficient D_{int} . The reason is that the faster grain boundary diffusion coefficient governs the time of arrest but not the propagation distance which is governed by the complex interaction between hydrogen transport and material deformation as the crack advances. We emphasize here that our approach to simulating crack arrest does account for the fact that a decreasing applied stress intensity factor enables crack arrest. In fact, our simulations of crack arrest do reflect the interaction of a continuously decreasing applied stress intensity with a decreasing grain boundary cohesion according to our proposed thermodynamic model of decohesion.

Figure 11.12 shows crack growth vs. time curves for two values of the exponent m , 10 and 12. The graphical representation of the relevant Eq. (11.28) is shown in the figure inset. We notice that a higher value of the parameter m is associated with a sharper decrease in the irreversible work of separation, and this in turn leads to a faster crack growth. We note that an increasing value of m or a decreasing value of κ has a similar effect on crack growth. In both cases the irreversible work of separation decreases and hence crack growth accelerates. The reason is that, for a given grain boundary concentration c_{int} , a large m yields a small work of separation $(w_p)_{c_{int}}$; a small κ yields indirectly a small $(w_p)_{c_{int}}$ by providing a small reversible work of separation $(2\gamma_{int})_{c_{int}}$.



11.12 Effect on crack propagation of the parameter m in the relation between irreversible work and reversible work of fracture. In both experiments and simulations, the specimen was bolt-loaded at $K_I^0 = 57.8 \text{ MPa } \sqrt{\text{m}}$ in hydrogen gas at pressure 207 MPa (external embrittlement). In the simulations, $(\Sigma_m)_0 = 20 \text{ GPa}$ and $D_{int} = D$.

11.2.6 Hydrogen transport exclusively through the grain boundary

Prompted by the difference between simulation and experimental results as shown in Figs 11.9 through 11.12, we explored a simplified version of the model. In this version, we assume: (i) the grain boundary diffusion coefficient can be orders of magnitude greater than the hydrogen diffusion coefficient in the bulk; (ii) thus, we ignore diffusion of hydrogen through the bulk material and this assumption removes the enforcement of the constraint Eq. (11.22) on the chemical potential continuity of hydrogen between bulk and grain boundary; (iii) grain boundary diffusion is driven only by concentration gradients, that is, we ignore the effect of grain boundary straining as depicted in the chemical potential of hydrogen by Eq. (11.8); and (iv) this way we decouple in the initial/boundary-value problem the effect of deformation on grain boundary diffusion. However, we do account for the effect of hydrogen on the cohesive properties of the grain boundary (traction-separation law) and hence on the interaction between crack propagation and elastic deformation in the bulk.

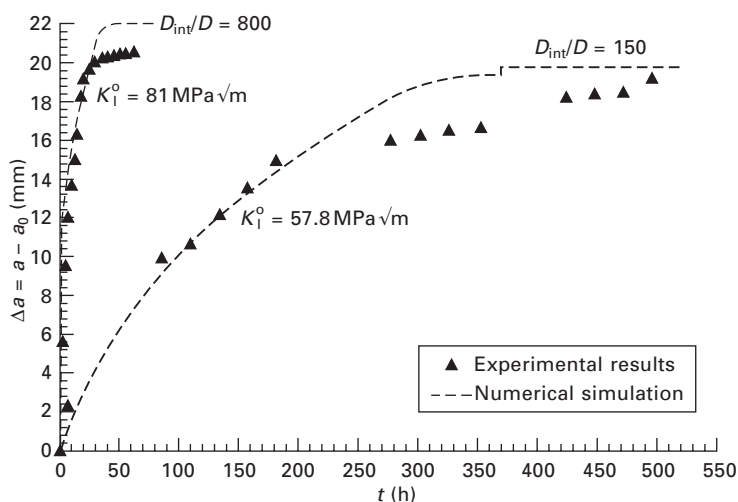
Figure 11.13 shows the simulation results superposed on the experimental results of Moody *et al.* [6, 7] for the crack propagation as a function of time. To get agreement between simulation and experiment, we used a grain

boundary diffusion coefficient that varies with the initially applied stress intensity factor K_I^0 . In other words, although we ignored the strain effect on the chemical potential of hydrogen on the grain boundary, we do bring into consideration a suggestion whereby a grain boundary experiencing larger straining may provide a faster diffusion path through the magnitude of the diffusion coefficient. We have no justification for this suggestion, but there is no experimental evidence refuting the idea of an increased diffusivity along a grain boundary strained in a crack tip environment and especially under a pressure of 207 MPa. Certainly, the agreement between experiment and simulation is rather surprising and as such it warrants further investigation of this decoupled model.

11.3 Subcritical ductile cracking: gaseous hydrogen exposure at pressures less than 45 MPa or internal hydrogen

11.3.1 Introduction

In this subsection, we model and simulate the final arrest stage of subcritical cracking in IN903 as observed by Moody *et al.* [6, 7] with WOL specimens. Subcritical cracking in this regime took place by void nucleation and growth at carbide particles for hydrogen gas pressures smaller than 45 MPa. We also



11.13 Simulation of crack propagation in hydrogen gas at pressure 207 MPa (external embrittlement) based only on concentration-driven grain boundary diffusion (no bulk diffusion). In the simulations, $(\Sigma_m)_0 = 20 \text{ GPa}$ and $m = 10$.

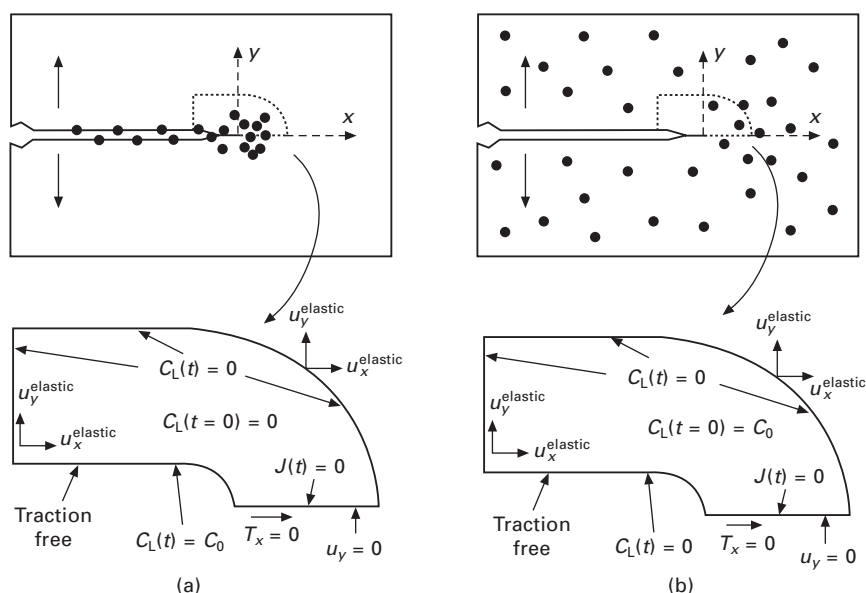
discuss a similar ductile failure scenario of precharged WOL specimens. The objective here is to analyze the role of hydrogen/microstructure interaction in IN903 upon crack arrest. Using a solid mechanics methodology, we explore the existence of a characteristic length scale that controls the fracture process and the possible correlation of this characteristic distance with material microstructural dimensions.

The experimental results of Moody *et al.* [6, 7] in the case of subcritical cracking in a gaseous environment are summarized in Table 11.4. The hydrogen concentrations are gas-phase equilibrium concentrations determined by accounting for the number of trapping sites at the matrix/ γ' -precipitate interfaces, the effective hydrogen fugacity, and the solubility of hydrogen in the lattice at 295 K. Thresholds were associated with no detectable crack growth after four months in hydrogen gas. Failure initiated by void nucleation at carbides whose average diameter D_0 and spacing were respectively 6.3 μm and 35.0 μm . The critical void size at failure, D_v/D_0 , was determined by measuring dimple diameters on the fracture surfaces just prior to the threshold stage.

As discussed, we expect that hydrogen-induced degradation in IN903 is confined very close to the crack tip, given the very small distances the hydrogen solute travels once absorbed from the environment. Hence, hydrogen interaction with material deformation is modeled under small scale yielding by focusing on the fracture process zone close to the crack tip. This small-scale yielding approach reduces the time required for the computations as the small scale yielding domain of analysis (see Fig. 11.14) is much smaller than the entire WOL specimen. Further, since we focus on the stress, strain, and hydrogen concentration field interactions only at crack arrest, the simulations are for a static crack. The reason we analyze the static crack upon arrest rather than the propagating crack is twofold: (i) we only have experimental data on void size just prior to crack arrest and (ii) even if we had such void size data during crack propagation, our finite element technologies on modeling hydrogen-induced failure by void growth and coalescence under transient

Table 11.4 Experimental data for ductile subcritical crack growth in IN903 in hydrogen gas. The hydrogen concentration denotes crack face concentration in both trapping and NILS sites in equilibrium with hydrogen gas. The parameter D_0 denotes the diameter of the carbides at which voids nucleated

Hydrogen gas pressure (MPa)	Hydrogen concentration (appm)	Threshold stress intensity K_{th} (MPa $\sqrt{\text{m}}$)	Void diameter at failure D_v/D_0
20.7	2735	49.0	1.36
20.7	2735	45.2	1.37
44.8	3355	42.5	1.36
44.8	3355	41.2	1.37



11.14 Schematic of the small scale yielding simulation domains along with boundary and initial conditions for (a) gaseous hydrogen uptake (external embrittlement) with a crack face equilibrium concentration C_0 ; and (b) pre-charging at an initial concentration of hydrogen C_0 (internal embrittlement).

hydrogen diffusion conditions are not yet robust. Ahn *et al.* [2] carried out such hydrogen-assisted ductile crack propagation by void growth, but under equilibrium hydrogen conditions since their analysis was for the A533B nuclear reactor steel, a ferritic system through which hydrogen diffuses fast and equilibrium can be easily attained.

An important issue with the model and simulation we propose for the static crack tip at arrest is that the history of the hydrogen diffusion and plastic dissipation in the wake of the propagating crack will not be accounted for. Also, we seek to understand the experimentally measured arrest threshold in relation to material microstructure exclusively on the basis of void growth. We omit the hydrogen effect on the void nucleation process since we have no experimental data to quantify it specifically for IN903. Hence, the present model and simulation results should be viewed in perspective, that is, the calculated threshold stress intensity factor is a conservative estimate as it ignores energy expenditure on the plastic wake and void nucleation.

The remainder of the chapter is organized as follows: the numerical model and simulation of the coupled hydrogen transport and material elastoplasticity problems are outlined in the next two subsections. Then, the approach to calculating the characteristic fracture distance is presented, followed by the finite element calculation results.

11.3.2 Elastoplastic deformation in the presence of hydrogen

It is well known that hydrogen facilitates dislocation motion at the microscale [54], thus inducing local material softening where hydrogen accumulates. To account for this softening effect from a continuum mechanics perspective, we resort to the work of Tabata and Birnbaum [55] who based on microscopic studies of the effect of hydrogen on dislocation behavior in iron concluded that the flow stress of the material decreased with increasing hydrogen concentration. Then, following Sofronis *et al.* [56], we propose that the local flow stress in the IN903 specimen is a function of the local hydrogen concentration

$$\sigma_Y(\varepsilon^p, c) = \sigma_0(c) \left(1 + \frac{\varepsilon^p}{\varepsilon_0} \right)^{\frac{1}{n}} \quad [11.33]$$

where $\sigma_0(c)$ is the yield stress, $c = (C_L + C_T)/N_L$ is the total hydrogen concentration in traps and NILS measured in hydrogen atoms per solvent atom, ε_0 is the yield strain in the absence of hydrogen, ε^p is the logarithmic strain in uniaxial tension, and n is the hardening exponent. A possible suggestion for $\sigma_0(c)$ is a linear form

$$\sigma_0(c) = \begin{cases} \left[(\xi - 1) \frac{c}{c_r} + 1 \right] \sigma_0 & \sigma_0(c) \geq 0.5\sigma_0 \\ 0.5\sigma_0 & \sigma_0(c) < 0.5\sigma_0 \end{cases} \quad [11.34]$$

where σ_0 is the yield stress in the absence of hydrogen, $\xi \leq 1$ is a parameter describing the extent of softening and c_r is a reference concentration such that when the total hydrogen concentration is $c = c_r$, $\xi = \sigma_0^H(c_r)/\sigma_0$ denotes the ratio of the yield stress in the presence of the hydrogen at concentration c_r to that in the absence of hydrogen. We assume that the hydrogen does not reduce the local flow stress by more than 50% in accordance with the observations by Tabata and Birnbaum [55] in iron. Eqs. (11.33) and (11.34) should be viewed just as a model approach at the continuum level to represent what is observed experimentally at the microscale. They reflect experimental observations of local flow stress reductions due to hydrogen induced shielding of dislocation/defect interactions. Although the notion of dislocation shielding in a complex microstructure such as the IN903 superalloy may appear questionable, it should be noted that the shielding mechanism has been experimentally observed to operate in a wide variety of engineering alloys, including the IN903 superalloy [54]. In fact, these equations can be used to represent the flow properties of the material in a point-wise fashion in the crack tip region given the point-wise varying hydrogen concentration field.

To obtain a 3-D version of the constitutive law for IN903, we assume isotropic linear elasticity and plasticity according to J_2 von-Mises yielding with isotropic hardening. Thus,

$$\overset{\nabla}{\sigma}_{ij} = 2G \left(\delta_{ik}\delta_{jl} + \frac{\nu}{1-2\nu} \delta_{ij}\delta_{kl} - \frac{3\sigma'_{ij}\sigma'_{kl}}{2(1+h/3G)\sigma_e^2} \right) (D_{kl} - D_{kl}^h) \quad [11.35]$$

for plastic loading and

$$\overset{\nabla}{\sigma}_{ij} = 2G \left(\delta_{ik}\delta_{jl} + \frac{\nu}{1-2\nu} \delta_{ij}\delta_{kl} \right) (D_{kl} - D_{kl}^h) \quad [11.36]$$

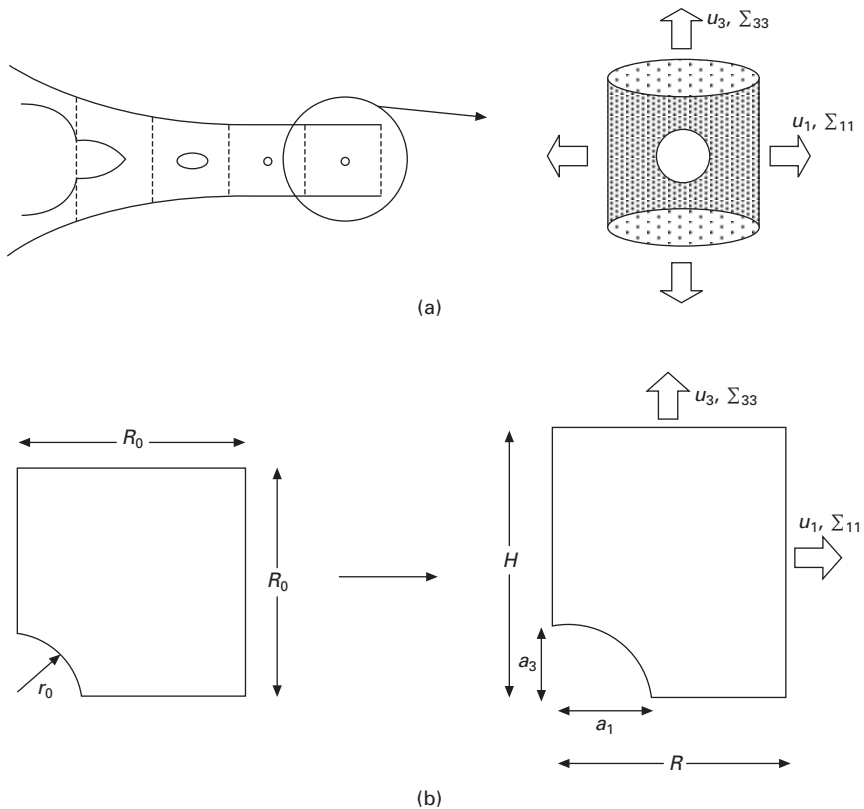
for elastic loading or unloading, where D_{ij} denotes the total deformation rate tensor equal to the symmetric part of the velocity gradient, $\overset{\nabla}{\sigma}_{ij}$ denotes the Jaumann rate of stress, $\sigma'_{ij} = \sigma_{ij} - (\sigma_{kk}/3)\delta_{ij}$ is the deviatoric stress, $\sigma_e = \sqrt{3\sigma'_{ij}\sigma'_{ij}/2}$ is the equivalent stress, G and ν are the shear modulus and Poisson ratio respectively, and $h = d\sigma_e/d\varepsilon^p$ is the slope of the uniaxial Cauchy stress vs. the logarithmic plastic strain ε^p which in multiaxial deformation is defined as $\varepsilon^p = \int \sqrt{2D_{ij}^p D_{ij}^p / 3} dt$. The hydrogen-induced lattice dilatation rate D_{ij}^h is given by Eq. (11.26).

11.3.3 The model

To develop a micromechanical model for the description of the hydrogen effect on void growth, one can use micromechanical unit cell calculations in which the cell is loaded by macroscopic stresses corresponding to a given applied stress triaxiality. Ahn *et al.* [57] and Liang *et al.* [58] carried out such calculations using respectively materials parameters for A533B steel and niobium to determine the hydrogen effect on void growth and coalescence through the constitutive law described by Eqs. (11.34) through (11.36). Such calculations yield the magnitudes of the macroscopic effective plastic strain and triaxiality at which a void grows to a given size. Using these micromechanical results and the experimental information for the critical void size at failure, we calculate the combinations of stress triaxiality and plastic strain under which a void can be brought to its critical size at failure as given by Table 11.4. Superposing these critical values of stress triaxiality and plastic strain over the profiles of the stress triaxiality and plastic strain ahead of the crack tip at the threshold stress intensity factor, we deduce the characteristic distance involved in the fracture process, that is, the characteristic distance over which voids can attain the critical size measured upon crack arrest.

For the micromechanical calculations, we consider an axisymmetric unit cell with a spherical void having nucleated from a carbide inclusion at its center (Fig. 11.15(a)). We assume the height and radius of the unit cell in the undeformed state to be equal to the carbide spacing $2R_0$ and the diameter of the void equal to the size $2r_0$ of the carbides. Due to symmetry, we analyze only a quadrant of the unit cell (Fig. 11.15(b)). The macroscopic stresses – which simulate the stress environment the void experiences at any given location ahead of the arrested crack – in the radial and axial directions are Σ_{11} and Σ_{33} , respectively, and the shear tractions on the outer surface are zero. During deformation, the height H and the radius R of the unit cell increase or decrease while the cell remains cylindrical. We define the radial and axial macroscopic strains respectively as $E_{11} = \ln(R/R_0)$ and $E_{33} = \ln(H/R_0)$, and the effective strain as

$$E_e = |E_{11} - E_{33}| \quad [11.37]$$



11.15 Schematic of the unit cell geometry and loading for the void growth calculations.

We approximate the shape of the deformed void as ellipsoidal and denote its half-axis lengths in the radial and axial directions by a_1 and a_3 , respectively. The stress triaxiality the cell experiences is

$$T = \Sigma_m / \Sigma_e \quad [11.38]$$

where Σ_e and Σ_m are respectively the macroscopic effective and hydrostatic stresses defined by

$$\Sigma_e = |\Sigma_{33} - \Sigma_{11}| \quad \Sigma_m = \frac{1}{3}(\Sigma_{33} + 2\Sigma_{11}) \quad [11.39]$$

We load the unit cell while we hold the triaxiality constant through a Newton iteration scheme [58]. We carry out the calculations using the finite element general purpose code ABAQUS with a user subroutine UMAT that incorporates the material constitutive model we presented in the previous subsection. In the calculations, we assume that hydrogen around the void is in equilibrium with local stress and plastic strain given the short diffusion distances involved for the local redistribution of hydrogen within the cell domain.

11.3.4 Numerical results

The material properties of IN903 are given in Table 11.1 [6, 7]. Traps are associated with the γ' precipitate/matrix interfaces and their density is equal to 0.005 atom fraction, that is, $N_T = 4.3023 \times 10^{26}$ traps/m³. We carried out the simulations at a temperature of 295 K, as in the experiments. In all calculations, we set the softening parameter ξ and reference concentration c_r equal to 0.927 and 500 appm, respectively. These values of ξ and c_r are associated with a 40% reduction of the yield stress at the nominal total hydrogen concentration of 2735 appm. The choice of this reference magnitude for the hydrogen concentration is based on the fact that it is quite different from the maximum concentrations attained in the unit cell and thus Eq. (11.34) yields a mild gradation for the softening effect by hydrogen.

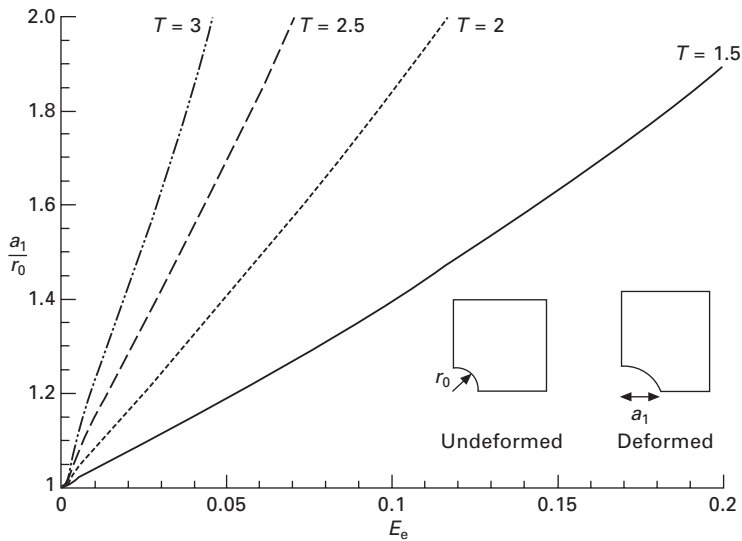
Gaseous hydrogen uptake (environmental embrittlement)

For the solution of the coupled hydrogen-transport/material-elastoplasticity problem at the crack tip loaded in hydrogen gas, we follow the approach of Dadfarnia *et al.* [59] under small scale yielding conditions. At time zero, we assume there is no hydrogen in the material (see Fig. 11.14(a)). In the absence of any H diffusion, we apply the macroscopic displacements incrementally at a constant stress intensity factor rate up to the final value corresponding to the threshold stress intensity K_{th} [60]. Then, while we keep the macroscopic displacements fixed at K_{th} , we switch on hydrogen diffusion through the crack faces and solve the coupled equations of hydrogen

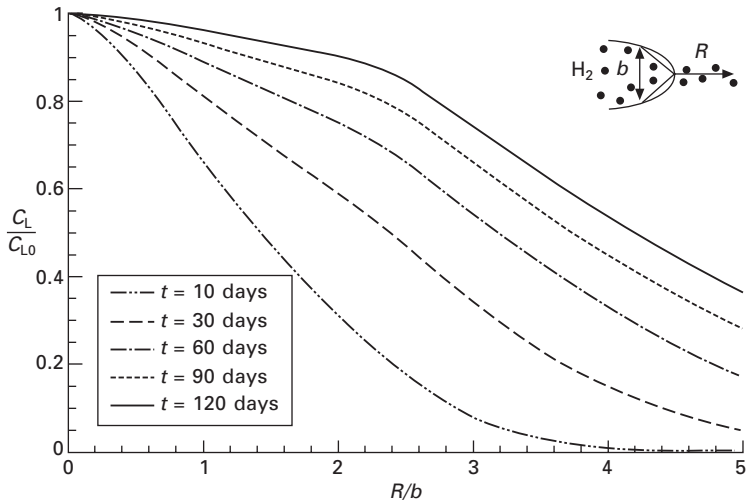
diffusion and material elastoplasticity by marching in time for four months – the time at which Moody *et al.* [6, 7] experimentally identified as arrest. The objective is to quantify the hydrogen effect on fracture by correlating the measured arrest threshold with the experimentally measured void sizes reported in Table 11.4.

Consider the case of crack growth in 20.7 MPa hydrogen gas (stress-free NILS concentration 349 appm, total stress-free hydrogen concentration 2735 appm) for which the void size at failure was $D_v/D_0 = 1.36$ and the measured threshold intensity factor was $K_{th} = 49 \text{ MPa}\sqrt{\text{m}}$ (first row of Table 11.4). The unit cell numerical results for the deformed void radius under different stress triaxialities are shown in Fig. 11.16. For a_1/r_0 equal to 1.36 (the experimental measurement) the predicted macroscopic plastic strain, Eq. (11.37), are 0.0921, 0.0449, 0.0260 and 0.0171, respectively for stress triaxialities of 1.5, 2, 2.5, and 3.

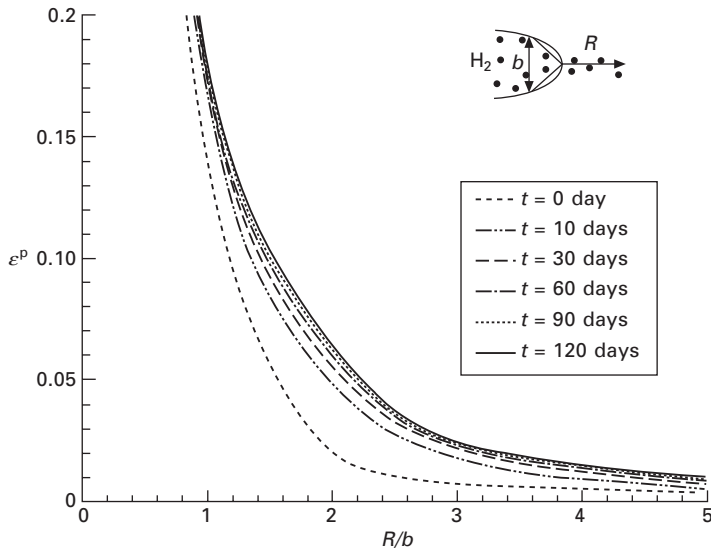
The simulation results for the profiles of hydrogen, plastic strain, hydrostatic stress, and stress triaxiality vs. normalized distance R/b from the crack tip are presented in Figs 11.17 through 11.20. The parameter b denotes the crack tip opening displacement and is defined through the 90° intersection method. We note that the crack tip opening displacement varies with time although the load is kept constant because the material continuously softens with hydrogen ingress. The time $t = 0$ corresponds to the switching on of the hydrogen diffusion. Figure 11.17 shows the evolution of the NILS hydrogen



11.16 Unit cell results of normalized void size (see Fig. 11.15) vs macroscopic effective strain E_e (Eq. 11.37) at various applied macroscopic stress triaxialities $T = \Sigma_{kk}/3\Sigma_e$ (Eq. 11.38).



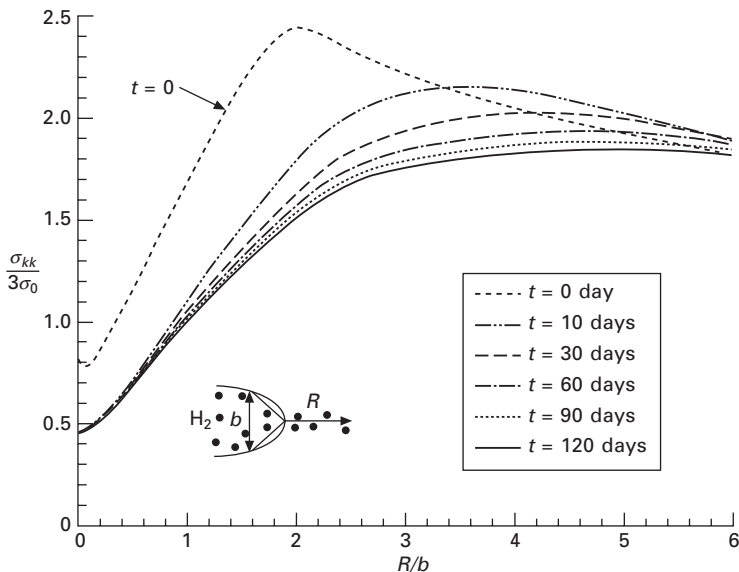
11.17 Evolution of the normalized NILS hydrogen concentration C_L/C_{L0} vs normalized distance R/b from the crack tip at threshold stress intensity $K_{th} = 49 \text{ MPa } \sqrt{\text{m}}$ in hydrogen gas at pressure 20.7 MPa (external embrittlement). The parameter b denotes the crack opening displacement at the corresponding time and $C_{L0} = 3.003 \times 10^{25} \text{ atoms/m}^3$ (349 appm) is the crack face NILS concentration in equilibrium with hydrogen gas.



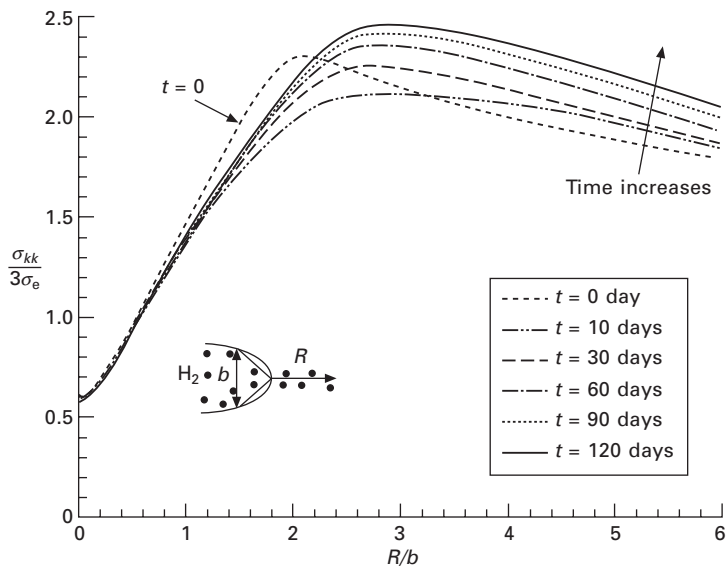
11.18 Evolution of effective plastic strain vs normalized distance R/b from the crack tip at threshold stress intensity $K_{th} = 49 \text{ MPa } \sqrt{\text{m}}$ in hydrogen gas at pressure 20.7 MPa (external embrittlement) as hydrogen diffuses into the material. The parameter b denotes the crack opening displacement at the corresponding time.

concentration ahead of the crack tip for times up to four months. During this longest time, hydrogen does not reach steady state, a case whereby the hydrogen concentration profile would exhibit a local maximum at the hydrostatic stress peak location ahead of the crack tip. Figures 11.18 and 11.19 present how the plastic strain and hydrostatic stress change in front of the crack tip. As hydrogen diffuses into the material and its concentration increases, the material in the neighborhood of the blunting crack tip softens, and this causes the plastic strain to increase and the hydrostatic stress to decrease. Also, as the hydrogen concentration increases, the peak of the hydrostatic stress moves further ahead of the crack tip due to the increasing extent of softening. Unlike hydrostatic stress, the triaxiality ahead of the crack tip increases (see Fig. 11.20) because the softening-induced reduction of the effective stress is larger than the reduction of the hydrostatic stress (cf. Eq. (11.38)).

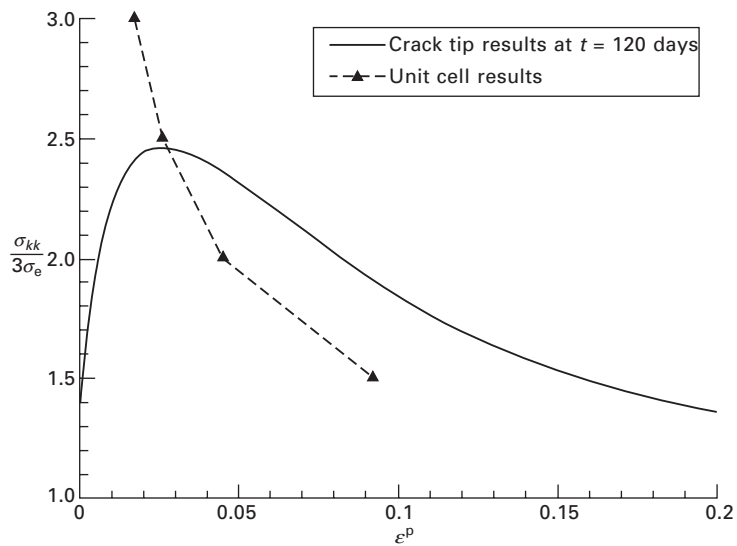
Using the results shown in Figs 11.18 and 11.20 at crack arrest ($t = 120$ days), one can plot the triaxiality and plastic strain prevailing at material points ahead of the crack at the time of the arrest as shown in Fig. 11.21. Superposed on this figure are also the data points from the unit cell calculations



11.19 Evolution of normalized hydrostatic stress vs normalized distance R/b from the crack tip at threshold stress intensity $K_{th} = 49 \text{ MPa} \sqrt{\text{m}}$ in hydrogen gas at pressure 20.7 MPa as hydrogen diffuses into the material. The parameter b denotes the crack opening displacement at the corresponding time and the yield stress in the absence of hydrogen is $\sigma_0 = 1081 \text{ MPa}$.



11.20 Local triaxiality $\sigma_{kk}/3\sigma_e$ vs normalized distance R/b from the crack tip at threshold stress intensity $K_{th} = 49 \text{ MPa}\sqrt{\text{m}}$ in hydrogen gas at pressure 20.7 MPa (external embrittlement) as hydrogen diffuses into the material. The parameter b denotes the crack opening displacement at the corresponding time.



11.21 Local triaxiality vs local plastic strain ahead of the crack tip at threshold stress intensity $K_{th} = 49 \text{ MPa}\sqrt{\text{m}}$ and superposed critical triaxiality vs. critical plastic strain from matching the unit cell calculation predictions on the void size with the experimentally measured values at K_{th} .

that denote combinations of triaxiality and plastic strain which can induce voids to grow to sizes which were measured in the experiment prior to crack arrest. The distance of the crossing point between these two curves from the crack tip identifies the size of the domain over which the critical strain and triaxiality conditions are satisfied for the voids to have the size measured prior to crack arrest. Obviously this characteristic distance denotes the fracture process zone for hydrogen-induced onset of crack initiation. For 20.7 MPa hydrogen gas pressure and threshold intensity $K_{th} = 49 \text{ MPa}\sqrt{\text{m}}$, we calculated this characteristic distance to be $l^* = 34.5 \mu\text{m}$, given that the crack opening displacement at arrest is $b = 12.06 \mu\text{m}$.

Following the same procedure, one determines the characteristic fracture distance for all other cases (rows) reported in Table 11.4. The results of these calculations are summarized in Table 11.5. Clearly, the calculated characteristic distance from the crack tip can be identified with the average carbide spacing, which suggests that it is the carbide spacing that controls fracture initiation, and by inference crack arrest, in hydrogen gas pressures up to 44.8 MPa.

Precharged specimens (internal embrittlement)

Moody *et al.* [6, 7] monitored subcritical cracking of IN903 in hydrogen-precharged WOL specimens. Table 11.6 shows the experimentally measured arrest thresholds at various stress-free NILS hydrogen concentrations along with the experimentally measured void sizes at failure. In particular, at a stress-free NILS hydrogen concentration of 194 appm with an associated trapped hydrogen concentration of 1682 appm (total hydrogen concentration of 1876 appm), they found that the crack did not propagate for 30 days after arrest at a threshold stress intensity factor $K_{th} = 35.9 \text{ MPa}\sqrt{\text{m}}$. Figure 11.22 shows the transient NILS hydrogen profile ahead of the crack tip, simulated under small scale yielding (see Fig. 11.14b) over the time period of 30 days from the time of initial loading. The applied macroscopic displacements correspond to the threshold stress intensity factor. The dominant feature in

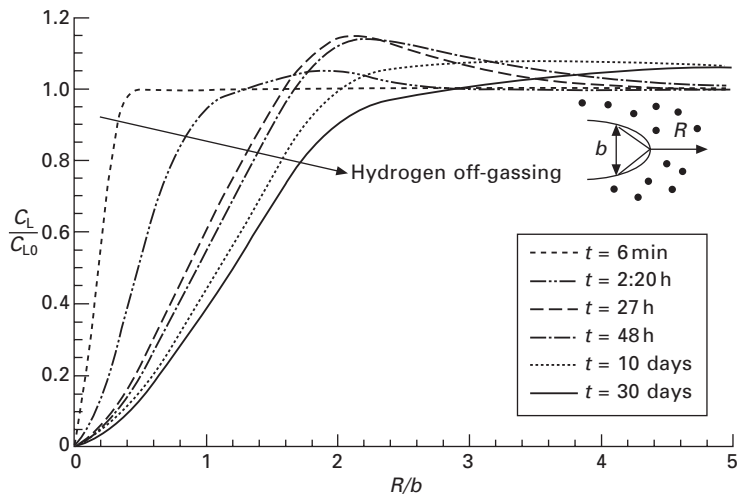
Table 11.5 Calculated characteristic distance controlling fracture in hydrogen gas (external embrittlement)

Hydrogen gas pressure (MPa)	Threshold stress intensity $K_{th} (\text{MPa}\sqrt{\text{m}})$	Characteristic fracture distance $l^* (\mu\text{m})$
20.7	49.0	34.5
20.7	45.2	30.7
44.8	42.5	33.9
44.8	41.2	32.4

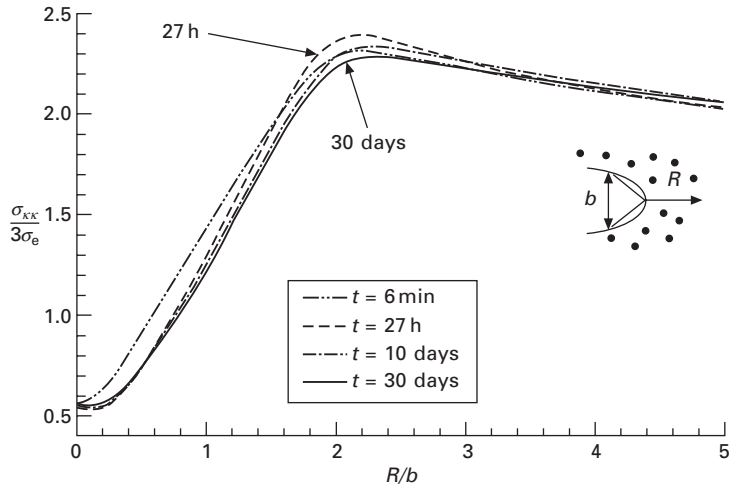
this case is hydrogen off-gassing from the crack tip which leads to a profile (see Fig. 11.22) that is radically different from the one shown for gaseous hydrogen in Fig. 11.17. Such a concentration profile yields the triaxiality profile shown in Fig. 11.23 and whose peak is closer to the crack tip than in the case of gaseous hydrogen since now the near tip region strengthens by the off-gassing of hydrogen. Close to the crack tip, $R/b < 1$, softening is weaker than in the case of gaseous hydrogen and this yields hydrostatic

Table 11.6 Experimental data and calculated characteristic distance controlling fracture for ductile subcritical crack growth in IN903 in precharged specimens (internal embrittlement). The hydrogen concentration denotes bulk concentration in both trapping and NELS sites before straining. The parameter D_0 denotes the diameter of the carbides at which voids nucleated

Experimental data			Numerical results
Hydrogen concentration (appm)	Threshold stress intensity K_{th} (MPa \sqrt{m})	Void diameter at failure D_v/D_0	Characteristic fracture distance l^* (μm)
1876	35.9	1.44	8.66
2900	26.3	1.34	10.3
5000	22.3	1.30	5.91



11.22 Evolution of the NELS hydrogen concentration C_L/C_{L0} vs normalized distance R/b from the crack tip at threshold stress intensity $K_{th} = 35.9 \text{ MPa } \sqrt{m}$ for precharged specimen (internal embrittlement). The parameter b denotes the crack opening displacement at the corresponding time and $C_{L0} = 1.669 \times 10^{25} \text{ atoms/m}^3$ (194 appm) is the initial NELS concentration before straining.



11.23 Local triaxiality $\sigma_{kk}/3\sigma_e$ vs normalized distance R/b from the crack tip at threshold stress intensity $K_{th} = 35.9 \text{ MPa} \sqrt{\text{m}}$ for pre-charged specimen (internal embrittlement). The parameter b denotes the crack opening displacement at the corresponding time.

stresses that increase with time. However, the triaxiality reduces with time because the von Mises effective stress increases at a faster pace than the hydrostatic stress decreases.

Repeating the same analysis we presented in the preceding subsection for the calculation of the characteristic distance for fracture, we summarize the results in Table 11.6. At this stage we have no physical interpretation for the magnitude of the characteristic distance for internal hydrogen embrittlement shown in Table 11.6. It may be the size of the carbide particle close to the crack tip that is responsible for the initiation of the void growth process that led to ductile cracking. Certainly more experimental data are needed to justify such an assertion.

11.4 Discussion

A general conclusion one may draw by assessing the experimental data of Moody *et al.* [6, 7] is that the *magnitude of the threshold stress intensity factor is sensitive to the hydrogen boundary and initial conditions*. The present simulations demonstrate that this sensitivity is dictated by the local crack tip environment. The crack tip environment is configured by the source of hydrogen and its interaction with the local plastic straining and stress triaxiality. We should add that part of the crack tip environment is also the presence of various hydrogen microstructural traps such as carbide particles, dislocations, and γ' precipitates.

11.4.1 Intergranular cracking

We modeled and simulated hydrogen-induced subcritical intergranular crack propagation in WOL specimens of iron-based IN903 bolt-loaded in high pressure (207 MPa) gaseous hydrogen. We used cohesive elements to model grain boundary decohesion as hydrogen diffused along the grain boundaries and degraded the cohesive stress. To describe the energetics of decohesion, we quantified the cohesive properties of the grain boundary on the basis of the thermodynamic theory of Mishin *et al.* [23]. We also used this framework to describe hydrogen diffusion along a grain boundary that undergoes separation. Experimental evidence suggests that intergranular cracking of IN903 in hydrogen does not take place in a completely brittle fashion. In fact, reviewing the literature on hydrogen-induced fractures, Ahn *et al.* [2] found that most hydrogen-induced fractures are accompanied by substantial dislocation activity. To account for the attendant shear processes, we modified the traction-separation law as was furnished by the thermodynamic theory for reversible decohesion. The modification is based on the theory of Jokl *et al.* [29] who were the first to propose a quantitative relationship between the true work of fracture and the ideal work of decohesion.

The numerical results suggest that a build-up of a critical hydrogen concentration plateau ahead of the crack tip is required for continued crack growth. After the crack propagates over a certain distance and the applied stress intensity factor decreases, the combination of local stresses and hydrogen diffusion cannot maintain the required plateau size of critical hydrogen accumulation necessary for continued crack advance. As a consequence, the crack arrests. This hydrogen-saturated plateau feature for subcritical cracking suggests that the size of the fracture process zone (plateau) changes continuously with time as the crack advances. Since such a model of fracture is counterintuitive, and given the fact that model ingredients were only included if justified experimentally, we conclude the following.

First, the plateau size is of the order of $10\text{ }\mu\text{m}$, when the cohesive stress of the grain boundary is 20 GPa. Such a fracture process zone size may be considered as extraordinarily large in light of the discussion advanced by Gangloff [5] who estimated the characteristic distance for fracture in IN903 to be submicron in size. A way to reduce the fracture process zone size further is to increase the grain boundary cohesive stress. However, we feel that assuming a cohesive stress magnitude larger than $18.5\sigma_0$, which is the value used in the simulations, is a magnitude we cannot justify in view of the lack of any direct experimental evidence. Similarly, we assumed a hydrogen-induced reduction of the ideal fracture energy no larger than 20%. Here, too, our thesis is that there is no direct evidence for more dramatic cohesion reductions.

Using the moving line source model of Johnson [61], we calculate the

steady state hydrogen concentration profile ahead of a propagating crack tip at constant velocity. For a crack tip radius $5.0\text{ }\mu\text{m}$ and propagating velocities smaller than 10^{-8} m/s , the Johnson approach yields distances from the crack tip over which the hydrogen concentration is substantial, i.e., greater than 0.05 appm, that are less than $1.7\text{ }\mu\text{m}$. The experimental data of Moody *et al.* [6, 7] are associated with velocities in this range. Analyzing the data, we find an average crack speed of $1.1 \times 10^{-8}\text{ m/s}$ for initial loading $K_I^0 = 57.8\text{ MPa}\sqrt{\text{m}}$ at time zero, and $9.5 \times 10^{-8}\text{ m/s}$ for $K_I^0 = 81.0\text{ MPa}\sqrt{\text{m}}$. If we account for the fact that trapping reduces the hydrogen diffusion coefficient by at least one order of magnitude, then we may deduce on the basis of the Johnson model that the characteristic diffusion distance in alloy IN903 is of submicron size. As we have already mentioned, Gangloff [5] already reached this conclusion regarding the magnitude of the characteristic distance for fracture in alloy IN903. Moreover, Gangloff [5] demonstrated that Stage II crack propagation velocities in high strength alloys scale with the hydrogen diffusion coefficient in the alloys after it is qualified for trapping. In particular, based on approximate steady state predictions for the hydrogen population enhancements ahead of a crack tip, Gangloff estimated that the fracture characteristic distance for IN903 is less than $10\text{ }\mu\text{m}$. It is worth noting here that in these estimations the effect of hydrogen-induced degradation on the transport of hydrogen was not accounted for. In contrast, in our model simulations, we come up with characteristic fracture distances larger than $10\text{ }\mu\text{m}$ partly because hydrogen diffusion does not take place only through NILS but also along a grain boundary whose opening accelerates the motion of hydrogen from the crack tip. While we do not see a problem with our predictions for the fracture process zone size under the present formulation of the hydrogen/deformation interaction, we do see a problem with the fact that the zone size needs to increase for continued crack advance, which at the moment remains unresolved. We may be tempted to attribute this inconsistency to the nature of the cohesive zone model approach whereby an ever-increasing number of cohesive elements needs to be involved in the decohesion process in order for the crack to advance (crack tip element to be completely separated) as the stress intensity factor reduces with crack propagation. This, if true, is certainly a computational artifact which is not related to any underlying physics of hydrogen-induced grain boundary decohesion. Further research is needed to elucidate this issue of robustness of the cohesive element approach to model and simulate environmental degradation.

Our numerical calculations with a cohesive stress $18.5\sigma_0$ and a 20% maximum hydrogen-induced reduction of the reversible work of fracture fail to predict the crack advance vs. time experimental data and the size of the fracture process zone. We note, however, that we predict a threshold stress intensity factor close to the experimentally measured one. On the other

hand, simulations in which the degree of coupling between deformation and diffusion was relaxed yielded surprisingly excellent agreement between the model predictions and the experimental data. This last approach needs further investigation.

11.4.2 Ductile cracking

We modeled and simulated hydrogen-induced ductile fracture in alloy IN903 under small scale yielding conditions as observed experimentally at the arrest stage of subcritical cracking in WOL specimens exposed either to a gaseous hydrogen atmosphere or being hydrogen precharged.

Using (i) the calculated stress and deformation fields ahead of the crack at threshold stress intensities upon crack arrest, (ii) unit cell calculations to describe the dependence of void growth on stress triaxiality, plastic straining, and hydrogen interaction with the matrix surrounding the void, and (iii) experimental data for the void sizes just before crack arrest, we found that critical void growth took place over a characteristic distance from the crack tip. This distance in the case of gaseous hydrogen uptake (external hydrogen embrittlement) was equal to the carbide spacing, 35 μm , independent of the charging pressure. On the other hand, the relevant characteristic distance for precharged specimens (internal hydrogen embrittlement) was about 8 μm which one may correlate to the carbide size. Certainly one can attribute the difference in the characteristic fracture distance between internal and external embrittlement to the different hydrogen concentration profiles (Figs 11.17 and 11.22) and the resulting corresponding difference in the interaction of hydrogen with the mechanism of void growth. Thus, an important conclusion is that *the characteristic fracture distance varies with the mode of hydrogen uptake and the fracture resistance certainly increases with increasing characteristic distance*. For the case of gaseous uptake, crack growth susceptibility is controlled by carbide spacing. The implication of this observation on the design of hydrogen compatible materials is obvious.

In the simulations with gaseous hydrogen uptake, we determined the hydrogen distribution ahead of the crack tip subjected to the threshold stress intensity factor by assuming no hydrogen throughout the simulation domain as an initial condition. As we have already mentioned, this is an idealization as hydrogen diffuses concurrently with crack propagation and there is certainly a pointwise varying concentration ahead of the crack tip when it reaches the arrest location. Further developments in this area require the determination of the stress and deformation fields during crack growth promoted by the ductile mechanism observed experimentally in the presence of transient hydrogen transport.

11.5 Conclusions

We presented a thermodynamic model for the determination of the cohesive properties of grain boundaries as affected by the presence of hydrogen solutes. Based on this model for reversible decohesion, we evaluated the irreversible work of fracture through the theory suggested by Jokl *et al.* [29]. We simulated hydrogen-induced intergranular fracture in WOL iron–base superalloy IN903 specimens in a hydrogen environment by accounting for transient hydrogen transport and material deformation/degradation. The model and simulation results are summarized as follows:

- The hydrogen-induced degradation of grain boundary cohesion was considered a function of the local hydrogen concentration with 20% maximum reduction of the cohesive energy at saturation. This model assumption is in line with *ab initio* calculation results for an almost ideal grain boundary model.
- The magnitude of the threshold stress intensity factor is governed by the local crack tip stresses and hydrogen environment, and it depends on the mode of hydrogen uptake.
- The simulations through cohesive finite elements reveal a fracture process zone that increases with continued crack propagation under decreasing applied stress intensity. The zone contains a hydrogen saturation plateau ahead of the crack tip and its size depends on the cohesive stress of the grain boundary. For a cohesive stress of 20 GPa, the plateau size is about 10 μm .
- Although simulations yielded threshold stress intensities close to the experimental values, they fell short of predicting crack growth rates.
- Crack arrest is the case when the synergism of tensile opening stress and hydrogen diffusion ahead of the crack tip cannot maintain the required plateau size of critical hydrogen accumulation for continued crack advance.

We modeled and simulated hydrogen-induced ductile fracture in WOL specimens of IN903 under small scale yielding conditions. The specimens either were exposed to a gaseous hydrogen atmosphere or were hydrogen precharged. Using (i) the calculated stress and deformation fields ahead of the crack at threshold stress intensities upon crack arrest, (ii) unit cell calculations to describe the dependence of void growth on stress triaxiality, plastic straining, and hydrogen interaction with the matrix surrounding the void, and (iii) experimental data for the void sizes just before crack arrest, we found that the fracture process is controlled by a characteristic distance. In particular,

- The characteristic fracture distance depends strongly on the mode of hydrogen uptake and the fracture resistance of the material to hydrogen embrittlement increases with increasing characteristic distance.

- For gaseous hydrogen uptake, the crack growth susceptibility is controlled by the carbide spacing.

11.6 Acknowledgments

The authors gratefully acknowledge support from the Los Alamos National Laboratory under US Department of Energy Contract No. LANL 62568-001-08 and from the US Department of Energy under Grant GO15045.

11.7 References

1. Robertson I M, Lillig D and Ferreira P J (2009), 'Revealing the fundamental processes controlling hydrogen embrittlement', in Somerday B P, Sofronis P and Jones R, *Effects of Hydrogen on Materials: Proceedings of the 2008 International Hydrogen Conference*, Materials Park, OH, ASM International, 22–37.
2. Ahn D C, Sofronis P and Dodds Jr. R H (2007), 'Modeling of hydrogen-assisted ductile crack propagation in metals and alloys', *Int J Fract*, **145**, 135–157.
3. Martin M L, Fenske J A, Liu G S, Sofronis P and Robertson I M (2010), 'On the formation and nature of quasi-cleavage fracture surfaces in hydrogen embrittled steels', *Acta Mater*, **59**, 1601–1606.
4. Gangloff R P (2009), 'Science-based prognosis to manage structural alloy performance in hydrogen', in Somerday B P, Sofronis P and Jones R, *Effects of Hydrogen on Materials: Proceedings of the 2008 International Hydrogen Conference*, Materials Park, OH, ASM International, 1–21.
5. Gangloff R P (2003), 'Diffusion control of hydrogen environment embrittlement in high strength alloys', in Moody N R, *Hydrogen Effects on Material Behaviour and Corrosion Deformation Interactions*, Warrendale, PA, TMS, 477–497.
6. Moody N R, Perra M W and Robinson S L (1988), 'Hydrogen pressure and crack tip stress effects on slow crack growth thresholds in an iron-based superalloy', *Scripta Metall*, **22**, 1261–1266.
7. Moody N R, Perra M W and Robinson S L (1990), 'Hydrogen-induced cracking in an iron-based superalloy', in Moody N R and Thompson A W, *Hydrogen Effects on Material Behavior: Proceedings of the 4th International Conference on Effect of Hydrogen on Behavior of Materials*, Warrendale, PA, TMS, 625–635.
8. Gangloff R P (2003), 'Hydrogen assisted cracking of high strength alloys', in Milne I, Ritchie R O and Karihaloo B, *Comprehensive Structural Integrity*, New York, NY, Elsevier Science, 31–101.
9. Gangloff R P (2008), 'Critical issues in hydrogen assisted cracking of structural alloys', in Shipilov S A, Jones R H, Olive J-M and Rebak R B, *Environment-induced Cracking of Materials: Chemistry, Mechanics and Mechanism*, Oxford, Elsevier, 141–165.
10. ASTM Standard E1681-03 (2003), *Standard Test Method for Determining a Threshold Stress Intensity Factor for Environment-Assisted Cracking of Metallic Materials*, <http://www.astm.org/Standards/E1681.htm>.
11. Nibur K A, Somerday B P, San Marchi C, Foulk J W, Dadfarnia M, Sofronis P and Hayden G A (2010), *Measurement and interpretation of threshold stress intensity factors for steels in high-pressure hydrogen gas*, SAND2010-4633, Sandia National Laboratories.

12. Dadfarnia M, Sofronis P, Somerday B P, Robertson I M, Liu J B and Johnson D D (2009), 'Modeling issues on hydrogen-induced intergranular cracking under sustained load', in Somerday B P, Sofronis P and Jones R, *Effects of Hydrogen on Materials: Proceedings of the 2008 International Hydrogen Conference*, Materials Park, OH, ASM International, 613–621.
13. Moody N R, Robinson S L, Myers S M and Greulich F A (1989), 'Deuterium concentration profiles in Fe–Ni–Co alloys electrochemically charged at room temperature', *Acta Metall.*, **37**, 281–290.
14. Needleman A (1987), 'A continuum model for void nucleation by inclusion debonding', *J Appl Mech.*, **54**, 525–531.
15. Liang Y and Sofronis P (2004), 'On hydrogen-induced void nucleation and grain boundary decohesion in nickel–base alloys', *J Eng Mater Technol.*, **126**, 368–377.
16. Serebrinsky S, Carter E A and Ortiz M (2004), 'A quantum-mechanically informed continuum model of hydrogen embrittlement', *J Mech Phys Solids*, **52**, 2403–2430.
17. Tvergaard V and Hutchinson J W (1992), 'The relation between crack growth resistance and fracture process parameters in elastic-plastic solids', *J Mech Phys Solids*, **40**, 1377–1397.
18. Ruggieri C, Panontin T L and Dodds Jr. R H (1996), 'Numerical modeling of ductile crack growth in 3-D using computational cell elements', *Int J Fract.*, **82**, 67–95.
19. Liang Y and Sofronis P (2003), 'Micromechanics and numerical modelling of the hydrogen-particle–matrix interactions in nickel–base alloys', *Modell Simul Mater Sci Eng.*, **11**, 523–551.
20. Liang Y and Sofronis P (2003), 'Toward a phenomenological description of hydrogen-induced decohesion at particle/matrix interfaces', *J Mech Phys Solids*, **51**, 1509–1531.
21. Hirth J P and Rice J R (1980), 'On the thermodynamics of adsorption at interfaces as it influences decohesion', *Metall Trans A*, **11**, 1501–1511.
22. Scheider I, Pfuff M and Dietzel W (2008), 'Simulation of hydrogen assisted stress corrosion cracking using the cohesive model', *Eng Fract Mech.*, **75**, 4283–4291.
23. Mishin Y, Sofronis P and Bassani J L (2002), 'Thermodynamic and kinetic aspects of interfacial decohesion', *Acta Mater.*, **50**, 3609–3622.
24. Dadfarnia M, Novak P, Ahn D C, Liu J B, Sofronis P, Johnson D D and Robertson I M (2010), 'Recent advances in the study of structural materials compatibility with hydrogen', *Adv Mater.*, **22**, 1128–1135.
25. Sofronis P and McMeeking R M (1989), 'Numerical analysis of hydrogen transport near a blunting crack tip', *J Mech Phys Solids*, **37**, 317–350.
26. Oriani R A (1970), 'The diffusion and trapping of hydrogen in steel', *Acta Metall.*, **18**, 147–157.
27. Novak P, Yuan R, Somerday B P, Sofronis P and Ritchie R O (2010), 'A statistical, physical-based, micro-mechanical model of hydrogen-induced intergranular fracture in steel', *J Mech Phys Solids*, **58**, 206–226.
28. Peisl H (1978), 'Lattice strains due to hydrogen in metals', in Alefeld G and Volkl J, *Hydrogen In Metals I, Topics in Applied Physics*, Berlin, Springer-Verlag, 53–74.
29. Jokl M L, Vitek V and McMahon Jr. C J (1980), 'A microscopic theory of brittle fracture in deformable solids: a relation between ideal work to fracture and plastic work', *Acta Metall.*, **28**, 1479–1488.
30. Lillig D B (2000), *Understanding the environmental sensitivity of Ni₃Al*, PhD Dissertation, University of Illinois at Urbana-Champaign, Urbana, IL.

31. Lee T C, Robertson I M and Birnbaum H K (1989), 'An HVEM *in situ* deformation study of nickel doped with sulfur', *Acta Metall*, **37**, 407–415.
32. Lin T, Evans A G and Ritchie R O (1986), 'A statistical model of brittle fracture by transgranular cleavage', *J Mech Phys Solids*, **34**, 477–497.
33. Teter D F, Robertson I M and Birnbaum H K (2001), 'The effects of hydrogen on the deformation and fracture of β -titanium', *Acta Mater*, **49**, 4313–4323.
34. Rice J R (1968), 'A path independent integral and approximate analysis of strain concentration by notches and cracks', *J Appl Mech*, **35**, 379–386.
35. San Marchi C, Somerday B P and Robinson S L (2007), 'Permeability, solubility and diffusivity of hydrogen isotopes in stainless steels at high gas pressures', *Int J Hydrogen Energy*, **32**, 100–116.
36. Wei R P and Gangloff R P (1989), 'Environmentally assisted crack growth in structural alloys: perspectives and new directions', in Wei R P and Gangloff R P, *Fracture mechanics: Perspectives and directions*, ASTM STP 1020, Philadelphia, ASTM, 233–264.
37. Robertson W M (1977), 'Hydrogen permeation and diffusion in Inconel 718 and Incoloy 903', *Metall Trans A*, **8**, 1709–1712.
38. Yao J and Cahoon J R (1988), 'Discussion of "Hydrogen induced grain boundary fracture in high purity nickel and its alloys – enhanced hydrogen diffusion along grain boundaries"', *Scripta Metall*, **22**, 1817–1820.
39. Kimura A and Birnbaum H K (1988), 'Hydrogen induced grain boundary fracture in high purity nickel and its alloys – enhanced hydrogen diffusion along grain boundaries', *Acta Metall*, **36**, 757–766.
40. Tsuru T and Latanision R M (1982), 'Grain boundary transport of hydrogen in nickel', *Scripta Metall*, **16**, 575–578.
41. Yao J and Cahoon J R (1991), 'Experimental studies of grain boundary diffusion of hydrogen in metals', *Acta Metall Mater*, **39**, 119–126.
42. Yao J and Cahoon J R (1991), 'Theoretical modeling of grain boundary diffusion of hydrogen and its effect on permeation curves', *Acta Metall Mater*, **39**, 111–118.
43. Yao J, Meguid S A and Cahoon J R (1993), 'Hydrogen diffusion and its relevance to intergranular cracking in nickel', *Metall Trans A*, **24**, 105–112.
44. Latanision R M, Compeau C R and Kurkela M (1984), 'Hydrogen permeation and embrittlement studies on metallic glasses', in Gibala R and Hehemann R F, *Hydrogen Embrittlement and Stress Corrosion Cracking*, Metal Park, American Society for Metals, 297–313.
45. Robertson W M (1973), 'Hydrogen permeation, diffusion and solution in nickel', *Z Metallkd*, **64**, 436–443.
46. Latanision R M and Kurkela M (1983), 'Hydrogen permeability and diffusivity in nickel and Ni–base alloys', *Corrosion*, **39**, 174–181.
47. Ladna B and Birnbaum H K (1987), 'SIMS study of hydrogen at the surface and grain boundaries of nickel bicrystals', *Acta Metall*, **35**, 2537–2542.
48. Mutschele T and Kirchheim R (1987), 'Segregation and diffusion of hydrogen in grain boundaries of palladium', *Scripta Metall*, **21**, 135–140.
49. Kirchheim R, Huang X Y and Mutschele T (1990), 'Interaction of hydrogen with internal interfaces', in Moody N R and Thompson A W, *Hydrogen Effects on Material behavior: Proceedings of the 4th International Conference on Effect of Hydrogen on Behavior of Materials*, Warrendale, PA, TMS, 85–98.
50. Sutton A P and Balluffi, R W (1995), *Interfaces in Crystalline Materials*, New York, Oxford University Press.

51. Sofronis P and Taha A (2000), 'Micromechanical modeling of hydrogen transport – a review', in Kane R D, *Environmentally Assisted Cracking: Predictive methods for risk assessment and evaluation of materials equipment, and structures*, ASTM STP 1401, West Conshohocken, PA, ASTM, 70–103.
52. Dadfarnia M (2009), *Micromechanics of hydrogen-induced crack initiation in pipeline steels and subcritical crack propagation*, PhD Dissertation, University of Illinois at Urbana-Champaign, Urbana, IL.
53. Somerday B P and Moody N R (2001), 'Micromechanical modeling of hydrogen-induced fracture modes in IN903', in Ravi-Chandar T, Kishi T, Ritchie R O, Yokobori Jr A T and Yokobori T, *Advances in Fracture Research, Proceedings of ICF10*, CD-proceedings, Elsevier Science, Oxford, UK, Paper No. ICF108920R.
54. Robertson I M (2001), 'The effect of hydrogen on dislocation dynamics', *Eng Fract Mech*, **68**, 671–692.
55. Tabata T and Birnbaum H K (1983), 'Direct observations of the effect of hydrogen on the behavior of dislocations in iron', *Scripta Metall*, **17**, 947–950.
56. Sofronis P, Liang Y and Aravas N (2001), 'Hydrogen induced shear localization of the plastic flow in metals and alloys', *Eur J Mech A-Solids*, **20**, 857–872.
57. Ahn D C, Sofronis P and Dodds Jr. R H (2007), 'On hydrogen-induced plastic flow localization during void growth and coalescence', *Int J Hydrogen Energy*, **32**, 3734–3742.
58. Liang Y, Ahn D C, Sofronis P, Dodds Jr. R H and Bammann D (2008), 'Effect of hydrogen trapping on void growth and coalescence in metals and alloys', *Mech Mater*, **40**, 115–132.
59. Dadfarnia M, Sofronis P, Somerday B P and Robertson I M (2008), 'On the small scale character of the stress and hydrogen concentration fields at the tip of an axial crack in steel pipeline: effect of hydrogen-induced softening on void growth', *Int J Mater Res*, **99**, 557–570.
60. Williams M L (1957), 'On the stress distribution at the base of a stationary crack', *J Appl Mech*, **24**, 109–114.
61. Johnson H H (1974), 'Hydrogen gas embrittlement', in Bernstein I M and Thompson A W, *Hydrogen in Metals: Proceedings of an International Conference on the Effects of Hydrogen on Materials Properties and Selection and Structural Design*, Metals Park, OH, ASM, 35–49.